Synchronized chaos in extended systems and meteorological teleconnections

Gregory S. Duane
Program in Atmospheric and Oceanic Sciences and Department of Astrophysical, Planetary, and Atmospheric Sciences, University of Colorado, Boulder, Colorado 80309
(Received 4 August 1997)

While synchronized chaos is familiar in low-order systems, the relevance of this paradigm to natural phenomena and spatially extended systems is questionable because of the time lags introduced by finite signal propagation speeds. A form of partially synchronized chaos is here demonstrated in a low-order numerical model of the coupled large-scale atmospheric circulation patterns in the northern and southern hemispheres. The model is constructed using a Green's function method to represent the time-lagged boundary forcing of the flow in each hemisphere by Rossby waves emanating from the opposite hemisphere. The two hemispheric subsystems are semiautonomous because Rossby waves cannot penetrate the tropics except in narrow longitudinal bands where the background winds are westerly. Each hemisphere has previously been described by a 10-variable model, derived from a spectral truncation of the barotropic vorticity equation. The model exhibits dynamical regimes corresponding to ''blocked'' and ''zonal'' atmospheric flow patterns in the hemisphere. Applying the same spectral truncation to the Green's functions that define the coupling, we construct a 28-variable model of the coupled flow on a planet with simplified geometry and background wind field. Partial synchronization is manifest in a significant tendency for the two hemispheric subsystems to occupy the same regime simultaneously. This tendency is observed in actual meteorological data. Partial synchronization of this form can be viewed as an extension of on-off intermittency in a system with a synchronization manifold, to a region of parameter space that is far from the bifurcation point at which this manifold loses stability. [S1063-651X(97)00912-4]

PACS number(s): 05.45.+b, 02.30.Jr, 92.60.Bh

I. INTRODUCTION

It is now well established that coupled low-order chaotic systems can fall into synchronized motion along their strange attractors under a variety of conditions. The best known configuration is probably that of Pecora and Carroll [1], who demonstrated synchronization of two identical systems, directionally coupled through the sharing of common dynamical variables, which drive both systems but are driven by only one. This phenomenon is seen, for instance, in a pair of Lorenz systems where the x or y variable of the driving system is inserted in the role of the x or y variable, respectively, of the driven system. Earlier work by Fujisaka and Yamada [2] and also by Afraimovich *et al.* [3] had examined synchronization in systems dissipatively coupled through a bidirectional control signal. For identical systems, the latter authors [3] found that, as the coupling is weakened, synchronization degrades through the increasingly frequent appearance of periods of desynchronization, timed chaotically, amidst other periods of synchronization.

Low-order chaotic synchronization has been found to be robust under a variety of sources of degradation. If the systems are nonidentical, *generalized synchronization*, in which the the state of one system is a function of the state of the other may result [4]. Experimental and theoretical studies have shown synchronization, or generalized synchronization, to be preserved in the presence of realistic noise levels in the coupling signal [5]. This has led to the proposal that chaotic synchronization could be useful in secure communications [6].

Missing from these studies is evidence that synchronized chaos pertains to natural phenomena. As low-order chaos, and the regularities observed in chaotic low-order systems, have led to insights and predictions regarding the behavior of extended systems, as in the case, for instance, of the Feigenbaum sequence or of the Lorenz system itself, it is to be hoped that the same would be true of low-order chaotic synchronization. But while the earlier investigators [2,3] suggested applications to fluids or continuous media, subsequent investigations focused on low-order or man-made systems, with the notable exception of synchronization in high-order, but discrete, neuronal networks [7,8]. A starting point for investigating synchronization in continuous systems might be a system with a twofold symmetry, rather than one envisioned as the continuum limit of a large number of chaotic oscillators to be synchronized collectively. This would allow a natural decomposition into two subsystems and so one might be able to exploit the low-order results directly. A principal difficulty remaining with such a configuration of extended systems is that, because information propagates at finite speed, not all paired degrees of freedom in the two systems can exchange information at once, as they do in the low-order models. [Very recently, Kocarev *et al.* [9] demonstrated synchronization in pairs of coupled partial differential equation (PDE) systems, but in one space dimension.] The central question becomes whether the various time lags can conspire to give robust synchronized evolution of the two individually chaotic systems, typically each with a power spectrum unbounded in frequency, or to give some vestige of synchronicity.

Trivially, any experimental apparatus that realizes low-order chaotic synchronization [1,10,11] demonstrates synchronization in an extended system. But here the rigidity of solid objects or the physical relevance of variables such as

current to describe collective motion eliminate the troublesome time lags. We wish to examine the possibility of synchronization in a pair of coupled fluid systems, each system consisting of a continuum of dynamically distinct parts.

To investigate synchronized chaos in fluids, we turn to meteorology, historically a source of inspiration in nonlinear dynamics, for a theoretical model that can readily be compared to observations. The nearly two-dimensional structure of the atmosphere allows a simple description of the dynamics through a low-order chaotic model that vacillates between weather regimes [12]. We apply this description to a system that can be naturally decomposed into two semiautonomous, but coupled subsystems. Correlations between the regimes occupied simultaneously by the two subsystems at various instants of time give a crude indication of synchronicity in the model. Specifically, the two subsystems are the northern and southern hemisphere midlatitude systems, which are semiautonomous because Rossby waves do not penetrate the tropical regions where upper-tropospheric winds are easterly, for reasons reviewed in Sec. III. The two subsystems are coupled through the relatively narrow regions in the tropics, the *westerly ducts*, where upper-tropospheric winds are westerly [13]. The large-scale weather regimes are *blocked flow* and *zonal flow*, the latter corresponding to the normal progression of weather patterns from west to east and the former corresponding to an obstruction of this progression, typically by a large high-pressure center [14]. A tendency for blocking to co-occur in the northern and southern hemispheres constitutes an interhemispheric *teleconnection*.

The subset of phase space for which the two modeled subsystems are in the same state constitutes an invariant *synchronization manifold*. That is, because the two systems are dynamically identical in the model, once they are synchronized they remain so. For couplings not involving time lags it has been shown that dynamics governed by a stable synchronization manifold will bifurcate into chaotically alternating periods of synchronization and desynchronization as the coupling is weakened [3,15], as noise is introduced [16,5,15], or as the symmetry between the subsystems is broken [15]. On-off synchronization is in fact a special case of on-off intermittency [17,18], a phenomenon occurring when an invariant manifold is slightly unstable, causing trajectories to spend long periods very close to the manifold, then to deviate from it wildly for a while, then return, and so on. The point of this paper is that the time lags that arise in coupled extended systems generate an extreme form of the same erratic behavior, but one in which a synchronization tendency is still discernible.

In the next section, we show that a time lag can be introduced in the coupling of a pair of Lorenz systems in the Pecora-Carroll configuration [1]. A short time lag generates on-off synchronization while longer lags give rise to regime correlations with no distinct periods of synchronization. This paper then analyzes the dynamics of the two coupled atmospheric flow systems, represented by standard low-order models as reviewed in Sec. III, and using a Green's function method to formulate the time-lagged coupling, to show that correlations of a similar type arise. As shown in Sec. IV, the coupling depends on the differences between the state variables of the systems, as previous authors [19] have suggested might occur for geophysical fluid systems in the absence of a specific model, but involves time integrals of these differences expressed more conventionally as new dynamical variables. The phase-space trajectories of this model, examined in Sec. V, contain no macroscopic segments that are very close to synchronization as in on-off intermittency, but still maintain an average distance from the synchronization manifold that is reduced as compared to the case of no coupling. The synchronization manifold thus affects the global dynamics of the coupled system. The coupled system is shown to reside in a portion of parameter space that is part of the on-off intermittent regime, but is further from the bifurcation point at which the invariant manifold loses stability than systems usually considered. One manifestation is a small correlation between the phase-space regimes of the two subsystems, corresponding to blocked or zonal flow. Such correlations are actually observed in meteorological data, presented in Sec. VI. We conclude that an extension of on-off synchronization to more remote regions of parameter space, with recognizable synchronization periods possibly absent, can underlie partially synchronized chaos in extended systems.

II. PARTIAL SYNCHRONIZATION OF CHAOTIC SYSTEMS WITH TIME-LAGGED COUPLING

An illustrative example of time-lagged coupling is the following configuration of two Lorenz systems in the variables X,Y,Z and X_1,Y_1,Z_1, respectively, coupled through the auxiliary variable S:

$$\dot{X}=\sigma(Y-X), \tag{1a}$$

$$\dot{Y}=\rho(X-S)-Y-(X-S)Z, \tag{1b}$$

$$\dot{Z}=-\beta Z+(X-S)Y, \tag{1c}$$

$$\dot{S}=-\Gamma S+\Gamma c(X-X_1), \tag{1d}$$

$$\dot{X}_1=\sigma(Y_1-X_1), \tag{1e}$$

$$\dot{Y}_1=\rho(X_1+S)-Y_1-(X_1+S)Z_1, \tag{1f}$$

$$\dot{Z}_1=-\beta Z_1+(X_1+S)Y_1. \tag{1g}$$

The dynamical variable S accumulates information about the difference between the states of the two Lorenz subsystems. As $\Gamma\rightarrow\infty$ in Eq. (1d), with $\dot{S}$ finite, $S\rightarrow c(X-X_1)$. In this limit, Eq. (1) reduces to

$$\dot{X}=\sigma(Y-X), \tag{2a}$$

$$\dot{Y}=\rho[(1-c)X+cX_1]-Y-[(1-c)X+cX_1]Z, \tag{2b}$$

$$\dot{Z}=-\beta Z+[(1-c)X+cX_1]Y, \tag{2c}$$

$$\dot{X}_1=\sigma(Y_1-X_1), \tag{2d}$$

$$\dot{Y}_1=\rho[cX+(1-c)X_1]-Y_1-[cX+(1-c)X_1]Z_1, \tag{2e}$$

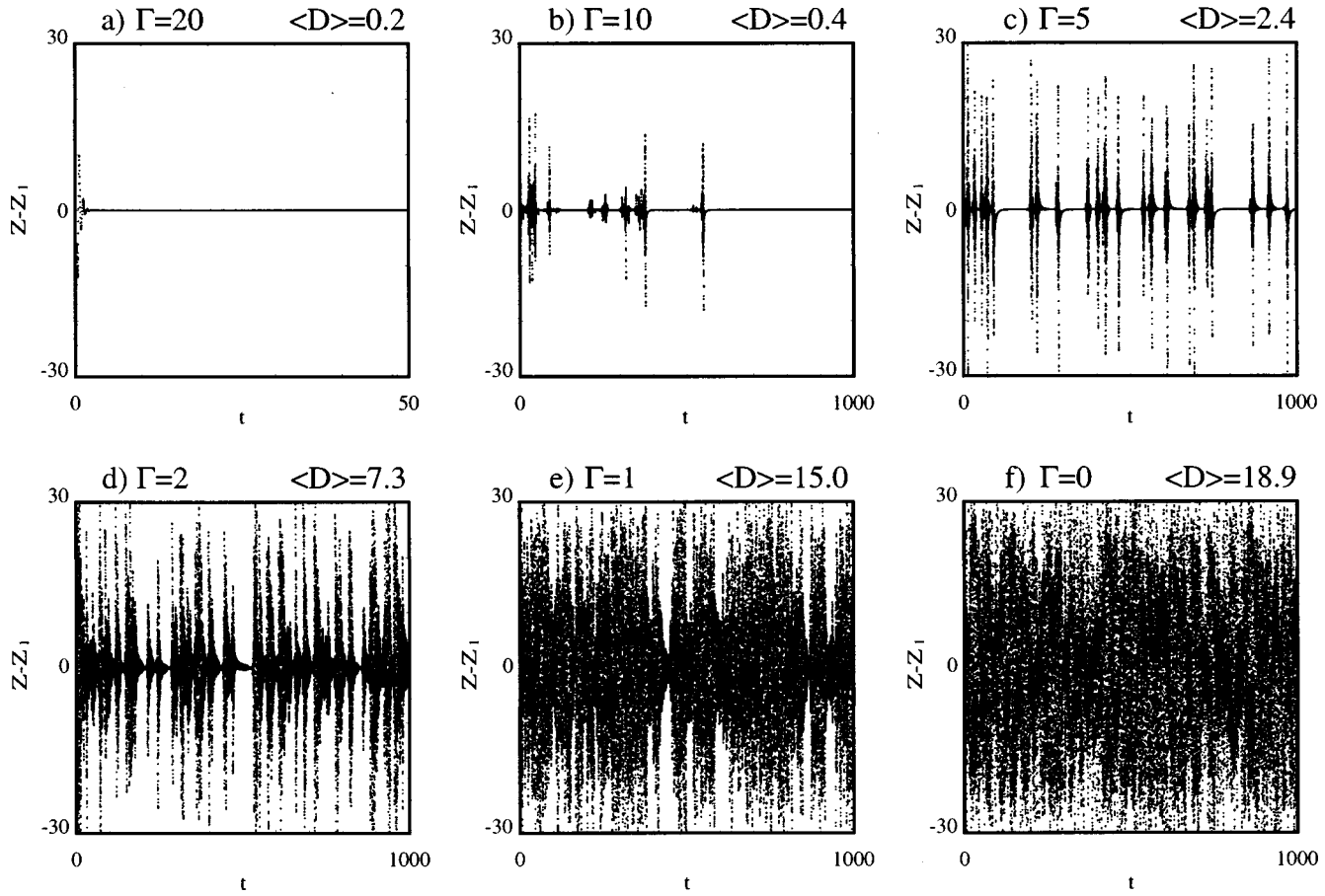

FIG. 1. The difference between the simultaneous states of two Lorenz systems with time-lagged coupling, as specified in Eq. (1), depicted by $Z(t)-Z_1(t)$ vs t for various values of the inverse time lag Γ. Average Euclidean distance $\langle D\rangle$ between the states of the two systems is also shown. The trajectories are generated by adaptive Runge-Kutta numerical integrations with $\sigma=10$, $\rho=28$, and $\beta=8/3$.

$$\dot{Z}_1=-\beta Z_1+[cX+(1-c)X_1]Y_1. \tag{2f}$$

The system (2) is a generalization of the Pecora-Carroll coupling scheme [1] to a case with bidirectional coupling and where each subsystem is partially driven and partially autonomous, with the degree of autonomy given by the quantity $1-c$. It is readily confirmed that this configuration synchronizes, for a range of values of c, including $c=1$, by direct simulation.

In the general case of the coupled system (1) with finite Γ, the subsystems exchange information more slowly: if X and X_1 are slowly varying, then S asymptotes to $c(X-X_1)$, over a time scale $1/\Gamma$. Thus, while c may be interpreted as the degree of coupling, Γ is an inverse time lag in the coupling dynamics.

Trajectories of Eq. (1) are depicted in Fig. 1 through $Z(t)-Z_1(t)$, for $c=1$ and decreasing values of Γ. For large Γ, the case represented in Fig. 1(a), the subsystems synchronize. As Γ is decreased in Figs. 1(b)–1(d), corresponding to increased time lag, increasingly frequent bursts of desynchronization are observed, until in Fig. 1(e) no portion of the trajectory is synchronized. The bursting behavior can be understood as an instance of on-off intermittency [18,17], the phenomenon that may occur when an invariant manifold containing an attractor loses stability, so that the attractor is no longer an attractor for the entire phase space, but is still effective in portions of the phase space. Trajectories then spend finite periods very close to the invariant manifold, interspersed with bursts away from it. (Experimental evidence of on-off intermittency in an extended physical system has been reported in a context not involving synchronization [20].) As has been pointed out by others [16,5,15], varying the dynamics of a system possessing a stable synchronization manifold that contains a strange attractor so as to destabilize this manifold may give rise to this phenomenon. Here, we enlarge the class of dynamical systems possessing a synchronization manifold to include ones with time-lagged coupling as in Eq. (1), and show that the time lag is yet another parameter that may be varied to induce instability.

A quantitative measure of the deviation of the behavior of the system at large time lag from on-off synchronization is provided by the average Euclidean distance $\langle D\rangle$ between the states of the two subsystems, where

$$D\equiv\sqrt{(X-X_1-2S)^2+(Y-Y_1)^2+(Z-Z_1)^2}$$

so that $D/\sqrt{2}$ is the distance of the system as a whole from the synchronization manifold. $\langle D\rangle$ is also shown in Fig. 1 for the various time lags. It is seen that $\langle D\rangle$ for the case of no macroscopic periods of synchronization in Fig. 1(e) is still less than $\langle D\rangle$ for the case of decoupled systems, shown in Fig. 1f. The former case, where $\Gamma=1$, is the physically rel-

TABLE I. (a) The joint probability matrix for the trajectory shown in Fig. 1(e) of the time-lagged coupled Lorenz systems specified in Eq. (1), where the regimes are given by $X>0$ ($X_1>0$) and $X<0$ ($X_1<0$). $P_{i,j}$ is the probability that the coupled model occupies a regime given by row i and column j. (b) The joint probabilities $P^{\rm ind}_{i,j}$ for *independent* subsystems, each with the same probability of occupying either regime as in (a), i.e., $P^{\rm ind}_{i,j}=(\Sigma_{j=+,-}P_{i,j})(\Sigma_{i=+,-}P_{i,j})$, with the regime correlation $\mathcal{C}$ as defined in Eq. (3).

	(a) P		(b) $P^{\rm ind}$	
	$X>0$	$X<0$	X>0	X<0
$X_1>0$	0.50	0.13	0.39	0.23
$X_1<0$	0.13	0.24	0.23	0.24
		$\mathcal{C}=0.44$		

evant situation in which the time scale of the delay due to the coupling is the same as the time scale of the intrinsic dynamics of the subsystems. The partial synchronization observed in this situation is thus seen to be related to the more familiar case of partial synchronization through on-off intermittency, but occurs further from the point in parameter space at which the synchronization manifold loses stability than systems usually considered.

Another measure of partial synchronization is provided by correlation between the gross regimes simultaneously occupied by the two subsystems. In the case of large time lag, shown in Fig. 1(e), where there are no macroscopic periods of synchronization, regime correlations can still be observed. The regimes are the two halves of the butterfly-shaped attractor of the Lorenz system, defined by $X<0$ and $X>0$. The co-occurrence statistics can be expressed as joint probabilites $P_{i,j}$—defined as the fraction of total time that the two subsystems spend in any pair of regimes i,j, respectively, where $i=+$ or $-$, $j=+$ or $-$. The matrix $P_{i,j}$ for the trajectory shown in Fig. 1(e) is given in Table I. Also given are the corresponding probability values $P^{\rm ind}_{i,j}$ in the case where the two subsystems individually have the same statistics but are assumed independent, i.e., $P^{\rm ind}_{i,j}=(\Sigma_{r=+,-}P_{i,r})(\Sigma_{s=+,-}P_{s,j})$. The joint probability matrix is significantly more diagonal than in the case of independent subsystems. The standard correlation between the two binary-valued random variables Q and R, which label the regimes of the two subsystems, is defined as $\mathcal{C}\equiv\langle(Q-\langle Q\rangle)(R-\langle R\rangle)\rangle/(\sigma_Q\sigma_R)$, where $Q=1$ ($R=1$) when $X>0$ ($X_1>0$) and $Q=0$ ($R=0$) otherwise. The correlation can also be expressed in terms of the joint probabilities as

$$\mathcal{C}\equiv\frac{P_{++}-P^{\rm ind}_{++}}{\sqrt{\sum_{r=-,+}P_{-,r}\sum_{r=-,+}P_{+,r}\sum_{s=-,+}P_{s,-}\sum_{s=-,+}P_{s,+}}}. \tag{3}$$

A significant positive correlation is observed for the case analyzed in Table I. This is but one manifestation of the effect of the synchronization manifold on the global dynamics of the system, even in the absence of periods of near synchronization. The remainder of this paper is devoted to showing that correlations similarly come about in a pair of coupled extended systems.

III. BACKGROUND: METEOROLOGICAL REGIMES AND LOW-ORDER MODELS

A. Blocking regimes in the general atmospheric circulation

Low-order spectral truncations of the primitive equations of quasi-two-dimensional fluid dynamics, on a rotating sphere with varying bottom topography, are known to capture the qualitative features of the large-scale atmospheric circulation in middle latitudes. In this section, we review the construction of one such low-order model, due to de Swart [12]. The starting point is the *barotropic vorticity equation*, which states that in a vertically homogeneous atmosphere, vorticity is conserved except when vortices are compressed by advection over topographic features or dissipated by bottom friction. This equation is

$$\frac{\partial(\nabla^2\Psi)}{\partial t}+J(\Psi,\nabla^2\Psi+f)+\gamma J(\Psi,h)+C\nabla^2(\Psi-\Psi^*)=0, \tag{4}$$

where Ψ is the stream function, which gives the x and y components of horizontal velocity $u=-\partial\Psi/\partial y$, $v=\partial\Psi/\partial x$, t is time, f is twice the locally vertical component of the rotation vector, which defines the Coriolis force, h is bottom topographic height, H is the average height of the atmosphere, $\gamma=f_0h_0/H$ is a coefficient of topographic forcing, f_0 is a typical value of f, h_0 is a topographic height scale, and C is a coefficient of bottom friction. The forcing stream function Ψ^* represents the flow forced by the equator-pole temperature gradient, which would define an equilibrium state in the absence of topographic effects. The advection Jacobian J is defined as

$$J(A,B)\equiv\frac{\partial A}{\partial x}\frac{\partial B}{\partial y}-\frac{\partial A}{\partial y}\frac{\partial B}{\partial x}, \tag{5}$$

so that the co-moving, or ''Lagrangian,'' derivative can be expressed as $D/Dt=\partial/\partial t+J(\Psi,\cdot)$. The second term in Eq. (4) thus gives the advection of total vorticity, which is the sum of *relative vorticity* $\zeta\equiv\partial u/\partial y-\partial v/\partial x=\nabla^2\Psi$ and *planetary vorticity* f. A detailed derivation of Eq. (4), with an explanation of the approximations used, can be found in [21].

We represent the mid-latitude system as a narrow channel between two circles of latitude, of width B (in the meridional, or y, dimension) and length L (in the zonal, or x, dimension), with periodic boundary conditions in x, and with the conditions at the northern and southern boundaries that the meridional wind v and the circulation $\int u\,dx$ vanish, i.e.,

$$\frac{\partial\Psi}{\partial x}=0,\quad y=0\text{ or }y=\pi b, \tag{6a}$$

$$\int\frac{\partial\Psi}{\partial y}dx=0,\quad y=0\text{ or }y=\pi b, \tag{6b}$$

where we have nondimensionalized x and y by defining a length scale $L/2\pi$ and we have introduced the nondimensional constant $b \equiv 2B/L$. The second boundary condition (6b) is necessary since while Eq. (6a) implies that Ψ is constant along the boundaries, Eq. (6a) taken alone permits this constant to vary in time. [The specific condition (6b) can be justified by integrating $u_t + uu_x + vu_y - fv = -(1/\rho)p_x - Cu + Cu^*$ (where subscripts denote derivatives), which follows from the Navier-Stokes equations with dissipation and forcing terms added, along each boundary, noting $v = 0$. Assuming the ''forcing velocity'' $u^* \equiv -\Psi_y^*$ itself has a vanishing boundary integral, the total circulation $\Omega \equiv \int u dx$ satisfies $\Omega_t = -C\Omega$, so that Ω decays to zero.] We further assume that f varies linearly with y in the channel, with $\partial f/\partial y = \beta$. The time t is nondimensionalized by defining a time scale equal to 10^5 s $= 1.16$ days, giving a nondimensional β of order unity.

A six-component spectral truncation of the barotropic vorticity equation (4) has been shown by Charney and DeVore [22] to exhibit multiple equilibria corresponding to different weather regimes in the atmosphere, following the approach of Lorenz, who applied the same expansion to more complex dynamical equations describing a two-layer model [23]. More recently, de Swart [12] showed that a corresponding 10-component spectral truncation of Eq. (4) exhibits chaotic behavior [12] with a strange attractor that gives vacillation between regimes. de Swart projected onto eigenfunctions Φ_j of the Laplacian operator in the channel defined above with boundary conditions (6). A complete set of such eigenfunctions is defined by $\Phi_j = \Phi_{j_1,j_2}$ for j_1 an integer and j_2 a positive integer:

$$\Phi_{0,j_2} = \sqrt{2}\cos\left(j_2 \frac{y}{b}\right), \tag{7a}$$

$$\Phi_{j_1,j_2} = \sqrt{2}e^{ij_1 x}\sin\left(j_2 \frac{y}{b}\right). \tag{7b}$$

The corresponding eigenvalues λ_j defined by $\nabla^2 \Phi_j = -\lambda_j \Phi_j$ [where $j = (j_1, j_2)$] are found to be $\lambda_j = {j_1}^2 + {j_2}^2/b^2$. The $j_1 = 0$ modes consist of purely zonal flow ($v = -\partial \Phi_{0,j_2}/\partial x = 0$), while the $|j_1| > 0$ modes consist of Rossby waves that are traveling in x and standing in y. That is, the mode Φ_{j_1,j_2} multiplied by a temporal factor $e^{-i\omega t}$, where

$$\omega = \frac{-\beta j_1}{\lambda_j} = \frac{-\beta j_1}{j_1^2 + (j_2/b)^2} \tag{8}$$

satisfies Eq. (4) with $h = C = \Psi^* = 0$, defining a Rossby wave [21] when $j_1 \neq 0$.

The expansion of the stream function Ψ, the forcing ''stream function'' Ψ^*, and the topography h in the basis (7) is defined by

$$(\Psi, \Psi^*, h) = \sum_j (\psi_j, \psi_j^*, h_j)\Phi_j. \tag{9}$$

The projection of the barotropic vorticity equation (4) onto the eigenfunctions (7) is found to be

$$\dot{\lambda}_j \dot{\psi}_j = \frac{1}{2}\sum_{l,m} c_{jlm}(\lambda_l - \lambda_m)\psi_l \psi_m + \gamma \sum_{l,m} c_{jlm}\psi_l h_m + \sum_l b_{jl}\psi_l - C\lambda_j(\psi_j - \psi_j^*), \tag{10}$$

where

$$c_{jlm} \equiv \frac{1}{2\pi^2 b}\int \overline{\Phi_j} J(\Phi_l, \Phi_m) dx dy,$$

$$b_{jl} \equiv \frac{1}{2\pi^2 b}\int \overline{\Phi_j} J(\Phi_l, f) dx dy,$$

with J denoting the advection Jacobian defined by Eq. (5) and overbars denoting complex conjugates. Equation (10) describes the time evolution of the coefficients of the expansion (7).

Assuming simple forms for the topography and forcing

$$h = \frac{1}{2\sqrt{2}}(\Phi_{1,1} + \Phi_{-1,1}) = \cos x \sin\frac{y}{b}, \tag{11}$$

$$\Psi^* = x_1^* \sqrt{2} b \cos\frac{y}{b} + x_4^* \sqrt{2} b \cos\frac{2y}{b}, \tag{12}$$

where x_1^* and x_4^* are constants, truncating Eq. (9) to $|j_1|, j_2 \leq 2$, and substituting an expansion in a real basis $\Psi = \Sigma_i x_i \Upsilon_i$ for the expansion (9), where $x_1 = \psi_{01}/b$, $x_2 = (\psi_{11} + \psi_{-11})/b\sqrt{2}$, $x_3 = i(\psi_{11} - \psi_{-11})/b\sqrt{2}$, $x_4 = \psi_{04}/b$, $x_5 = (\psi_{12} + \psi_{-12})/b\sqrt{2}$, $x_6 = i(\psi_{12} - \psi_{-12})/b\sqrt{2}$, $x_7 = (\psi_{21} + \psi_{-21})/b\sqrt{2}$, $x_8 = i(\psi_{21} - \psi_{-21})/b\sqrt{2}$, $x_9 = (\psi_{22} + \psi_{-22})/b\sqrt{2}$, $x_{10} = i(\psi_{22} - \psi_{-22})/b\sqrt{2}$, de Swart [12] obtained the dynamical system

$$\begin{aligned}
\dot{x}_1 &= \gamma_{11}^* x_3 - C(x_1 - x_1^*), \\
\dot{x}_2 &= -(\alpha_{11}x_1 - \beta_{11})x_3 - Cx_2 - \delta_{11}x_4 x_6 - \rho_{11}(x_5 x_8 - x_6 x_7), \\
\dot{x}_3 &= (\alpha_{11}x_1 - \beta_{11})x_2 - \gamma_{11}x_1 - Cx_3 + \delta_{11}x_4 x_5 + \rho_{11}(x_5 x_7 + x_6 x_8), \\
\dot{x}_4 &= \gamma_{12}^* x_6 - C(x_4 - x_4^*) + \epsilon_1(x_2 x_6 - x_3 x_5) + \epsilon_2 x_7 x_{10} - x_8 x_9, \\
\dot{x}_5 &= -(\alpha_{12}x_1 - \beta_{12})x_6 - Cx_5 - \delta_{12}x_3 x_4 + \rho_{12}(x_2 x_8 - x_3 x_7) + \gamma'_{12}x_8, \\
\dot{x}_6 &= (\alpha_{12}x_1 - \beta_{12})x_5 - \gamma_{12}x_4 - Cx_6 + \delta_{12}x_2 x_4 - \rho_{12}(x_2 x_7 + x_3 x_8) - \gamma'_{12}x_7, \\
\dot{x}_7 &= -(\alpha_{21}x_1 - \beta_{21})x_8 - Cx_7 - \delta_{21}x_4 x_{10} - \rho_{21}(x_2 x_6 + x_3 x_5) + \gamma'_{21}x_6,
\end{aligned} \tag{13}$$

TABLE II. The truncated basis that defines the de Swart model (13) of the single-hemisphere mid-latitude circulation, given by the stream function $\Psi=\Sigma_{i=1}^{10}x_i(t)\Upsilon_i$.

$\Upsilon_1=\sqrt{2}b\cos y/b$	$\Upsilon_2=2b\cos x\sin y/b$
$\Upsilon_3=2b\sin x\sin y/b$	$\Upsilon_4=\sqrt{2}b\cos 2y/b$
$\Upsilon_5=2b\cos x\sin 2y/b$	$\Upsilon_6=2b\sin x\sin 2y/b$
$\Upsilon_7=2b\cos 2x\sin y/b$	$\Upsilon_8=2b\sin 2x\sin y/b$
$\Upsilon_9=2b\cos 2x\sin 2y/b$	$\Upsilon_{10}=2b\sin 2x\sin 2y/b$

$$\dot{x}_8=(\alpha_{21}x_1-\beta_{21})x_7-Cx_8+\delta_{21}x_4x_9+\rho_{21}(x_2x_5-x_3x_6)-\gamma'_{21}x_5,$$

$$\dot{x}_9=-(\alpha_{22}x_1-\beta_{22})x_{10}-Cx_9-\delta_{22}x_4x_8,$$

$$\dot{x}_{10}=(\alpha_{22}x_1-\beta_{22})x_9-Cx_{10}+\delta_{22}x_4x_7,$$

with coefficients defined by

$$\alpha_{nm}=\frac{8\sqrt{2}n}{\pi}\frac{m^2}{4m^2-1}\frac{n^2b^2+m^2-1}{n^2b^2+m^2},$$

$$\beta_{nm}=\frac{\beta nb^2}{n^2b^2+m^2},$$

$$\gamma^*_{nm}=\frac{4m}{4m^2-1}\frac{\sqrt{2}nb\gamma}{\pi},$$

$$\gamma_{nm}=\frac{4m^3}{4m^2-1}\frac{\sqrt{2}nb\gamma}{\pi(n^2b^2+m^2)},$$

$$\gamma'_{nm}=\frac{3b\gamma}{4(n^2b^2+m^2)},$$

$$\delta_{nm}=\frac{64\sqrt{2}n}{15\pi}\frac{n^2b^2-m^2+1}{n^2b^2+m^2},$$

$$\epsilon_n=\frac{16\sqrt{2}n}{5\pi},$$

$$\rho_{nm}=\frac{9}{2}\frac{(n-2)^2b^2-(m-2)^2}{n^2b^2+m^2}. \tag{14}$$

For concreteness, we list the real basis functions explicitly in Table II.

A typical trajectory of the system (13) is represented in Fig. 2. Regime structure is manifest as different ranges of oscillation in different portions of the time series. A careful analysis [12] actually reveals three regimes, corresponding to three unstable fixed points, but two regimes are easily discerned in the figure. The value of the variable x_1 is sufficient to distinguish between these. The interpretation of weather phenomena in terms of vacillation among regimes has long been favored by meteorologists [14] and a three-regime scheme has indeed been proposed [24], in which the weather alternates between ''zonal flow'' periods of strong westerlies, a transitional regime, and a ''blocked'' regime in which a wavy flow pattern is typically associated with a persistent high pressure center that interferes with the flow of weather from west to east. Since $x_1=\psi_{01}/b$ is the coefficient of the lowest zonal-flow mode Φ_{01}, the regimes apparent in Fig. 2 were argued to correspond to zonal and blocked flow in the atmosphere [12]. To the author's knowledge, no higher order truncations of the barotropic vorticity equation (4) on a β plane have been investigated. (On a sphere, truncations of the barotropic vorticity equation which retain up to 25 modes have been investigated [25].) It has commonly been assumed that the low-order truncations capture the qualitative dynamics of the atmospheric regimes and transitions between them.

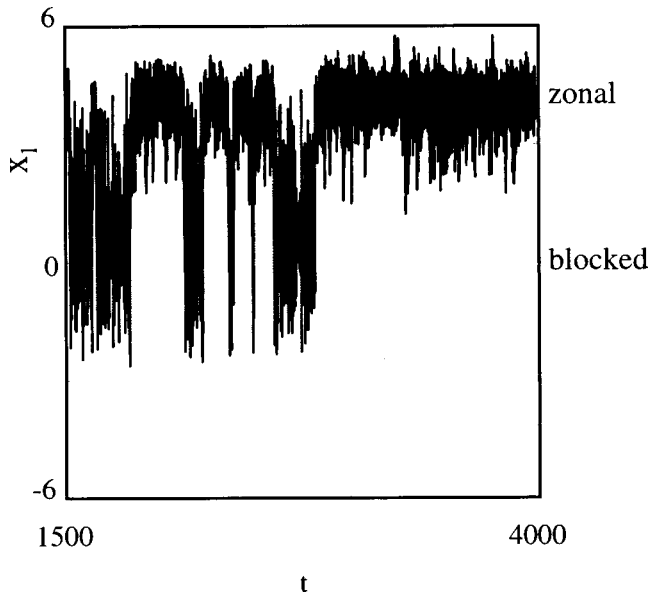

FIG. 2. A typical trajectory of the 10-component de Swart model [12] of the mid-latitude atmospheric circulation, specified by Eqs. (13). x_1 vs t is plotted for an adaptive Runge-Kutta numerical integration with $\beta=1.25$, $C=0.1$, $\gamma=1$, $b=1.6$, $x_1^*=4$, and $x_4^*=-8$. Only $t>1500$ (in nondimensional time units) is displayed so as to exclude transients.

B. Coupling of the mid-latitude systems through the tropical westerly ducts

Thus far we have not justified the boundary condition (6a), which defines the mid-latitude region as an autonomous system. The condition for the polar ($y=\pi b$) boundary may be regarded as resulting from the spherical geometry, and in any case will be unchanged in the two-hemisphere model to be described in the next section. On the other hand, the explanation of the tropical ($y=0$) boundary condition, which will be important for the formulation of the coupled model, rests on the existence of processes [not included in the simple model (4)] that maintain an average zonal wind at tropical latitudes [13]. It is found that this wind is typically easterly ($u<0$) in the tropics, in contrast to predominantly westerly ($u>0$) winds in the mid-latitude regions.

The effect of this band of tropical easterlies may be understood heuristically by considering the dispersion relation for Rossby waves [21] on a prescribed background state with

slowly varying winds [26]. Generalizing Eq. (8), in which the zonal and meridional wave numbers are $k=j_1$ and $l=j_2/b$, to the case in which there is a background wind $\overline{u}$, one finds

$$\omega=\overline{u}k-\beta k/(k^2+l^2),$$

which gives a zonal phase speed:

$$c_x=\overline{u}-\beta/(k^2+l^2). \tag{15}$$

Equation (15) implies that meridionally propagating waves ($c_x=0$) can only exist when $\overline{u}>0$ and more generally that waves can only exist when $\overline{u}-c_x>0$. Thus waves are permitted in the middle latitudes, in which a westerly $\overline{u}$ arises from the forcing by Ψ^*, but these waves must be either absorbed or reflected when they reach a critical line (different for each wave mode), near the tropical boundary, where $\overline{u}-c_x=0$. Since waves cannot exist in the region of tropical easterlies, and since the only nonwave modes consist of purely zonal flow, we must have $v=0$ in this region, hence Eq. (6).

Next we note that the band of tropical easterlies is sometimes broken by smaller regions of tropical westerlies over the Atlantic or Pacific oceans, each such region typically no more than 45° in longitudinal extent. Previous authors [13] have demonstrated that Rossby waves can penetrate through these *westerly ducts*, as illustrated in Fig. 3 for a numerical model more highly resolved than the models to be considered in this paper. To the extent that the boundary conditions (6) accurately represent the physical effects of the tropical easterly barrier, the same boundary conditions with holes can be used to construct a model of the two mid-latitude systems, coupled through the westerly ducts.

IV. THE COUPLED LOW-ORDER MODEL

To formulate the coupling between the two mid-latitude systems that is engendered by the transmission of Rossby waves through the westerly ducts, we neglect the meridional extent of the region of tropical easterlies, taking this region to be a line at the equator, and also assume that the two mid-latitude systems lie on a single β plane. (It can be verified that the latter assumption, which corresponds to f varying linearly with latitude everywhere, would be exact on a planet with a shape that is not spherical but that is also not terribly unrealistic.) The effect of the opposite hemisphere is that of a boundary forcing in the longitudinal range corresponding to the tropical westerly ducts. The forcing is given by replacing the boundary condition of zero meridional wind by the condition that meridional winds match across the tropical boundary, i.e., that $v(x,0^+)=v(x,0^-)$ in the duct regions, or equivalently that $\partial\Psi/\partial x$ matches across the boundary in these regions.

To isolate the effects of the boundary forcing in a linear equation that can be solved by conventional methods, we express the stream function Ψ as the sum of two parts: $\Psi=\Psi_0+\Psi_B$. The boundary-forced, or ''diffracted,'' part Ψ_B solves the linearized vorticity equation

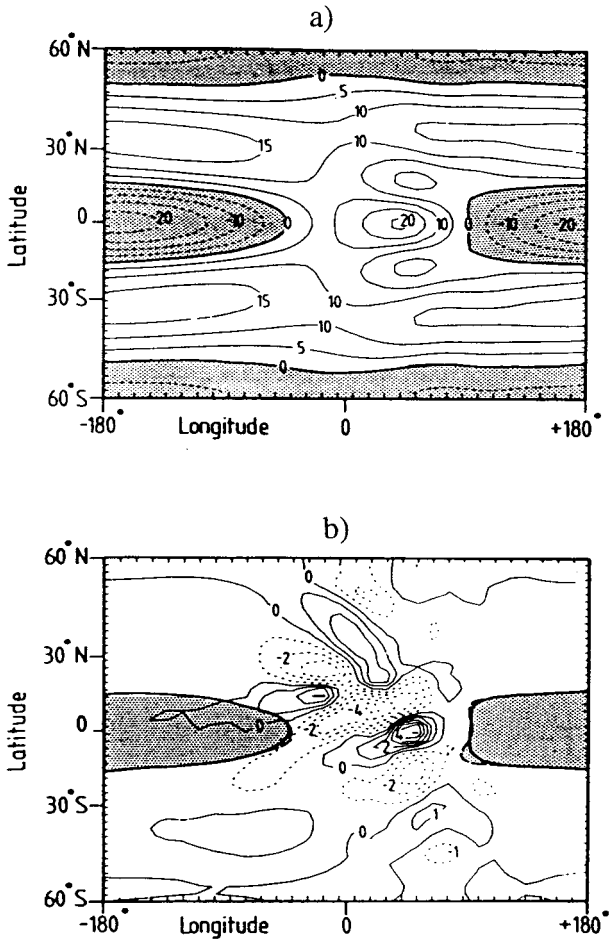

FIG. 3. Rossby-wave penetration of the tropical westerly ducts in a high-resolution numerical model of shallow-fluid dynamics [13]: (a) Contours of a prescribed basic state zonal wind field $\overline{u}$ (in m/s), intended to represent climatological conditions in the tropics. Regions of easterly wind $\overline{u}<0$ are shaded. (b) Contours of perturbation zonal wind u at $t=100$ days, with basic state as in (a), after initialization by a localized perturbation at 20° N at $t=0$ (reprinted from [13] by permission).

$$\frac{\partial(\nabla^2\Psi_B)}{\partial t}+J(\Psi_B,f)+C\nabla^2\Psi_B=0 \tag{16}$$

with matching boundary conditions, as described above, in the duct regions; the remaining free part Ψ_0 satisfies the Charney-DeVore boundary conditions (6) and is such that the total stream function Ψ satisfies the full vorticity equation (4). This decomposition is possible because the boundary conditions involve linear operators. Since $\partial\Psi_0/\partial x$ vanishes by definition, we must have $(\partial\Psi_B^N/\partial x)(x,0,t)=(\partial\Psi_B^S/\partial x)(x,0,t)$, valid both within and outside the duct regions, where the superscripts N and S will henceforth denote quantities in the Northern and Southern hemispheres, respectively. Shifting Ψ_B by an arbitrary constant in either hemisphere, we can require $\Psi_B^N(x,0,t)=\Psi_B^S(x,0,t)$. Also, Ψ_B must satisfy the condition (6b) on the circulation $\int u\,dx$ at the northern and southern boundaries. One boundary condition at the interface remains to be specified. Motivated by an analogy with optics, we posit a specific form for Ψ_B, the

''diffracted'' part of the stream function, on the tropical boundary: the stream function in the duct regions is set equal to the sum of the southward-propagating part of the flow north of the boundary and the northward-propagating part of the flow south of the boundary. That is,

$$\Psi_B^N(x,0,t)=\Psi_B^S(x,0,t)$$
$$=\left\{\begin{array}{ll} 0 & \text{outside ducts} \\ T\sum_j\,(\psi_j^N\Phi_j^{\downarrow}+\psi_j^S\Phi_j^{\uparrow}) & @\ \text{ducts}\end{array}\right\}$$
$$\equiv D(x,t), \tag{17}$$

where T is a parametric transmission coefficient, and the coefficients ψ_j^N and ψ_j^S are just the coefficients in the Charney-DeVore and de Swart spectral truncations of the full stream function in either hemisphere: $\Psi^{N,S}=\Sigma_j\psi_j^{N,S}\Phi_j^{N,S}$. The modes $\Phi_j^{N,S}$ are chosen so that the single-hemisphere equations derived from Eq. (10) will be the same on both sides of the equator. This requirement is met if the Rossby modes have the same form, while the zonal flow modes change sign, i.e.,

$$\Phi^S_{0,j_2}(x,y)=-\Phi^N_{0,j_2}(x,y), \tag{18a}$$

$$\Phi^S_{j_1,j_2}(x,y)=\Phi^N_{j_1,j_2}(x,y)\equiv\Phi_j(x,y),\quad j_1\neq 0. \tag{18b}$$

The northward- and southward-propagating parts of the Rossby modes $\Phi_j=\sqrt{2}e^{ij_1x}\sin(j_2y/b)$ $|j_1|,j_2>0$ are given by

$$\Phi_j=\Phi_j^{\uparrow}+\Phi_j^{\downarrow}, \tag{19a}$$

$$\Phi_j^{\uparrow}=\pm\frac{i}{\sqrt{2}}e^{ij_1x\mp ij_2y/b}, \tag{19b}$$

$$\Phi_j^{\downarrow}=\mp\frac{i}{\sqrt{2}}e^{ij_1x\pm ij_2y/b}, \tag{19c}$$

where the upper (lower) signs apply when $j_1>0$, $\omega_j<0$ (when $j_1<0$, $\omega_j>0$). The zonal flow modes $\Phi_{0,j_2}=\sqrt{2}\cos(j_2y/b)$ ($i=1$ or 4 in the de Swart model), with $\omega_j=0$, have no northward- or southward-propagating parts. Lastly, we also require that $\Psi_B=0$ at the exterior boundaries at $y=\pm\pi b$, which is equivalent (with $\Psi_B=0$ at $y=0$) to requiring that the instantaneous zonal circulation vanishes when averaged across the hemisphere. In summary, the boundary conditions satisfied by Ψ_B (in a domain that is periodic in x) are Eq. (17) and

$$\Psi_B^{N,S}=0,\quad y=\pm\pi b, \tag{20}$$

$$\int\frac{\partial\Psi_B^{N,S}}{\partial y}dx=0,\quad y=0,\pm\pi b. \tag{21}$$

The ansatz (17) will be shown to lead to a nondivergent solution to Eq. (4). It is intended to model the linear propagation of waves through the tropics that atmospheric scientists have used consistently at times [26,13] to describe the phenomenology of the large-scale circulation. Because of our assumptions regarding the shapes of the ducts and the background wind field, however, the sizes of the ducts and the transmission coefficient T are not to be taken literally and will remain open to interpretation. The coupling defined by Eq. (17) is illustrated schematically in Fig. 4.

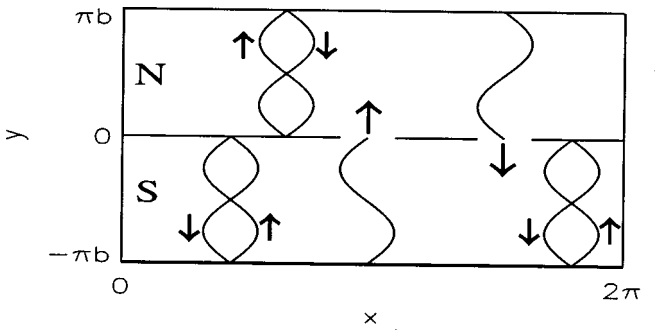

FIG. 4. Schematic diagram of the two-hemisphere coupled model. The tropical easterly barrier is assumed infinitely thin and both hemispheres are taken to lie on a single β plane. The two mid-latitude systems are boundary forced by the outward-propagating components of the meridionally standing wave modes in the opposite hemisphere.

Note that because of the symmetry of Eq. (16) (for $f=\beta y$), with the boundary condition (17):

$$\Psi_B^N(x,y,t)=\Psi_B^S(x,-y,t) \tag{22}$$

so we will henceforth refer only to one diffracted stream function $\Psi_B(x,y,t)\equiv\Psi_B^N(x,y,t)$.

To find Ψ_B from the boundary condition (17) we use the method of boundary Green's functions [27]. In this method, a Green's function that might have been used to solve an inhomogeneous equation with homogeneous boundary conditions is transformed to another type of Green's function that can be used to solve the corresponding homogeneous equation with inhomogeneous boundary conditons. This latter function, the boundary Green's function G^b, must exist because the linearity of Eq. (16) and the fact that initial conditions at $t=-\infty$ can be ignored due to the dissipative term, implies that Ψ_B must depend linearly on the boundary values, given in this case by the quantity D in (17). That is

$$\Psi_B(\mathbf{r},t)=\int_{t_0<t}D(x_0,t_0)G^b(\mathbf{r},t|x_0,t_0)dx_0dt_0 \tag{23}$$

[where $\mathbf{r}=(x,y)$ and $\mathbf{r}_0=(x_0,y_0)$]. As discussed in [27], there is usually a simple relationship between the boundary Green's function G^b and the ordinary Green's function G, which in the present case satisfies

$$\frac{1}{C}\frac{\partial(\nabla^2G)}{\partial t}+\frac{1}{C}J(G,f)+\nabla^2G=\delta^2(\mathbf{r}-\mathbf{r}_0)\,\delta(t-t_0) \tag{24}$$

with the causal boundary condition $G(\mathbf{r},t|\mathbf{r}_0,t_0)=0$ for $t<t_o$, and with homogeneous spatial boundary conditions:

$$G=0,\quad y=0\text{ or }y=\pi b, \tag{25a}$$

$$\int\frac{\partial G}{\partial y}dx=0,\quad y=0\text{ or }y=\pi b. \tag{25b}$$

The relationship between G^b and G in the present case turns out to be

$$G^b(x,y,t|x_0,t_0) = -\left(1+\frac{1}{C}\frac{\partial}{\partial t}\right)\left[\frac{\partial G(\mathbf{r},t|\mathbf{r}_0,t_0)}{\partial y_0}\right]_{y_0=0} \tag{26}$$

as proved in Appendix A.

A spectral expansion of the Green's function can now be combined with a spectral expansion of the stream function to yield a low-order model upon truncation. The governing equation is obtained by subtracting the linearized vorticity equation (16) from the full vorticity equation (4), yielding

$$\frac{\partial(\nabla^2\Psi_0^{N,S})}{\partial t} + J(\Psi_0^{N,S},f) + J(\Psi^{N,S},\nabla^2\Psi^{N,S}) + \gamma J(\Psi^{N,S},h) + C\nabla^2(\Psi_0^{N,S}-\Psi^*) = 0, \tag{27}$$

where $\Psi_0^{N,S}$ satisfies homogeneous boundary conditions (6), and

$$\Psi^N(x,y,t) = \Psi_0^N(x,y,t) + \Psi^B(x,y,t),$$
$$\Psi^S(x,y,t) = \Psi_0^S(x,y,t) + \Psi^B(x,-y,t) \tag{28}$$

and Ψ_B is given by the Green's function relation (23) in terms of the boundary values (17) of $\Psi^{N,S}$. The topography h has the same form, given by Eq. (11), in both hemispheres on our model planet, and there is no seasonal cycle. The forcing stream function Ψ^*, given by Eq. (12), has the same symmetry as the zonal flow modes (18a):

$$\Psi^{*S} = -\Psi^{*N} = -x_1^*\sqrt{2}b\cos\frac{y}{b} - x_4^*\sqrt{2}b\cos\frac{2y}{b}.$$

A complete set of orthonormal functions satisfying Eq. (25) are the eigenmodes (7b) of the Laplacian. [The zonal flow modes in (7a) are excluded by boundary condition (25a).] Therefore, we must have

$$G(\mathbf{r},t|\mathbf{r}_0,t_0) = \sum_{j_1\neq 0} A_j\Phi_j(\mathbf{r})$$

for some coefficients $A_j = A_j(t,\mathbf{r}_0,t_0)$, where as before $j=(j_1,j_2)$. Using the orthonormality relation for the eigenmodes Φ_j

$$\frac{1}{2\pi^2 b}\int \overline{\Phi_j}(\mathbf{r})\Phi_k(\mathbf{r})\,dx\,dy = \delta_{jk}$$

(where the overbar again denotes the complex conjugate) and using the fact that the eigenmodes given by Eq. (7) are also eigenfunctions of the operator $\partial/\partial x$, it can be verified that the function

$$G(\mathbf{r},t|\mathbf{r}_0,t_0) = -\theta(t-t_0)C\frac{1}{2\pi^2 b}\sum_{j_1\neq 0}\frac{\overline{\Phi_j}(\mathbf{r}_0)\Phi_j(\mathbf{r})}{\lambda_j} \times \exp[(-i\omega_j - C)(t-t_0)] \tag{29}$$

satisfies Eq. (24) as required, where θ is the step function

$$\theta(x) = \begin{cases} 1, & x \geqslant 0 \\ 0, & x < 0. \end{cases}$$

As before, $\omega_j = -j_1\beta/\lambda_j$ and the quantities $\lambda_j = j_1^2 + j_2^2/b$ are the eigenvalues of $\nabla^2\Phi_j = -\lambda_j\Phi_j$. Therefore, by Eq. (26):

$$G^b(\mathbf{r},t|x_0,t_0) = -i\,\theta(t-t_0)\frac{1}{2\pi^2 b} \times \sum_{j_1\neq 0}\frac{\omega_j(\partial\overline{\Phi_j}/\partial y)(x_0,0,t_0)\Phi_j(\mathbf{r})}{\lambda_j} \times \exp[(-i\omega_j - C)(t-t_0)]. \tag{30}$$

Note that if we substitute Eq. (30) in the integral in Eq. (23) we get a sum of eigenmodes for homogeneous boundary conditions (multiplied by overlap integrals) as a purported solution to the linearized equation with inhomogeneous boundary conditions. Our method [27] will give errors in a boundary layer near the ducts that will narrow as we retain an increasing number of terms in the expansion.

We express the sum of eigenmodes that defines Ψ_B explicitly:

$$\Psi_B = \sum_{j_1\neq 0}\zeta_j(t)\Phi_j. \tag{31}$$

This sum is also seen to be over Rossby modes only by substitution of Eq. (30) in Eq. (23). The physical reason for the decoupling of the zonal flow modes (7a) is that $u = -\partial\Phi_j/\partial y$ for these modes at the interface, so they would not contribute to the spectral expansion of G^b in Eq. (30) regardless of the imposed boundary conditions, implying that the arbitrary choice $\Psi_B = G = 0$ along the boundaries outside the ducts was appropriate. Since the Rossby modes are odd in y, $\Psi_B(x,-y,t) = -\Psi_B(x,y,t)$, so Eq. (28) becomes simply

$$\Psi^N(x,y,t) = \Psi_0^N(x,y,t) + \Psi^B(x,y,t),$$
$$\Psi^S(x,y,t) = \Psi_0^S(x,y,t) - \Psi^B(x,y,t), \tag{32}$$

where we regard Ψ_B as a single analytic function over the whole domain.

Changing to the real bases $\{\Upsilon_i\}_i^{N,S}$ corresponding to the basis defined in Table II for the single-hemisphere case, we define the time-dependent coefficients x_i^N, x_i^S, and y_i:

$$\Psi_0^{N,S} = \sum_{i=1}^{N} x_i^{N,S}(t)\Upsilon_i^{N,S}, \tag{33a}$$

$$\Psi_B = \sum_{i=1}^{N} y_i(t)\Upsilon_i^N = \sum_{i=1}^{N} y_i(t)\Upsilon_i^S, \tag{33b}$$

since $y_1 = y_4 = 0$ and $\Upsilon_i^N = \Upsilon_i^S$ for $i \neq 1,4$, whence

TABLE III. The equations of the 28-component two-hemisphere model. The coefficients are as in the single-hemisphere model (14) except where specified as different in the two hemispheres by the superscripts N and S. The coupling coefficients $c_{i,k}$ are given in Table IV. $\hat{x}_i^N = x_i^N + y_i$ and $\hat{x}_i^S = x_i^S - y_i$, so the 28 variables are the 10 x_i^N, the 10 x_i^S, and the 8 y_i. (The frequencies are the positive quantities $\omega_2 = |\omega_{11}|$, $\omega_5 = |\omega_{12}|$, etc.)

$$
\begin{aligned}
\dot{x}_1^N &= & \gamma_{11}^{*N}\hat{x}_3^N & - C(x_1^N - x_1^{*N}) & & & \\
\dot{x}_2^N &= -\alpha_{11}x_1^N\hat{x}_3^N - \beta_{11}x_3^N & & - Cx_2^N & - \delta_{11}x_4^N\hat{x}_6^N & - \rho_{11}(\hat{x}_5^N\hat{x}_8^N - \hat{x}_6^N\hat{x}_7^N) & \\
\dot{x}_3^N &= \alpha_{11}x_1^N\hat{x}_2^N - \beta_{11}x_2^N & - \gamma_{11}^N\hat{x}_1^N & - Cx_3^N & + \delta_{11}x_4^N\hat{x}_5^N & + \rho_{11}(\hat{x}_5^N\hat{x}_7^N + \hat{x}_6^N\hat{x}_8^N) & \\
\dot{x}_4^N &= & \gamma_{12}^{*N}\hat{x}_6^N & - C(x_4^N - x_4^{*N}) & + \epsilon_1(\hat{x}_2^N\hat{x}_6^N - \hat{x}_3^N\hat{x}_5^N) & + \epsilon_2(\hat{x}_7^N\hat{x}_{10}^N - \hat{x}_8^N\hat{x}_9^N) & \\
\dot{x}_5^N &= -\alpha_{12}x_1^N\hat{x}_6^N - \beta_{12}x_6^N & & - Cx_5^N & - \delta_{12}\hat{x}_3^N x_4^N & + \rho_{12}(\hat{x}_2^N\hat{x}_8^N - \hat{x}_3^N\hat{x}_7^N) & + \gamma_{12}'^N\hat{x}_8^N \\
\dot{x}_6^N &= \alpha_{12}x_1^N\hat{x}_5^N - \beta_{12}x_5^N & - \gamma_{12}^N x_4^N & - Cx_6^N & + \delta_{12}\hat{x}_2^N x_4^N & - \rho_{12}(\hat{x}_2^N\hat{x}_7^N + \hat{x}_3^N\hat{x}_8^N) & - \gamma_{12}'^N\hat{x}_7^N \\
\dot{x}_7^N &= -\alpha_{21}x_1^N\hat{x}_8^N - \beta_{21}x_8^N & & - Cx_7^N & - \delta_{21}x_4^N\hat{x}_{10}^N & - \rho_{21}(\hat{x}_2^N\hat{x}_6^N + \hat{x}_3^N\hat{x}_5^N) & + \gamma_{21}'^N\hat{x}_6^N \\
\dot{x}_8^N &= \alpha_{21}x_1^N\hat{x}_7^N - \beta_{21}x_7^N & & - Cx_8^N & + \delta_{21}x_4^N\hat{x}_9^N & + \rho_{21}(\hat{x}_2^N\hat{x}_5^N - \hat{x}_3^N\hat{x}_6^N) & - \gamma_{21}'^N\hat{x}_5^N \\
\dot{x}_9^N &= -\alpha_{22}x_1^N\hat{x}_{10}^N - \beta_{22}x_{10}^N & & - Cx_9^N & - \delta_{22}x_4^N\hat{x}_8^N & & \\
\dot{x}_{10}^N &= \alpha_{22}x_1^N\hat{x}_9^N - \beta_{22}x_9^N & & - Cx_{10}^N & + \delta_{22}x_4^N\hat{x}_7^N & &
\end{aligned}
$$

$$
\begin{aligned}
\dot{x}_1^S &= & \gamma_{11}^{*S}\hat{x}_3^S & - C(x_1^S - x_1^{*S}) & & & \\
\dot{x}_2^S &= -\alpha_{11}x_1^S\hat{x}_3^S - \beta_{11}x_3^S & & - Cx_2^S & - \delta_{11}x_4^S\hat{x}_6^S & - \rho_{11}(\hat{x}_5^S\hat{x}_8^S - \hat{x}_6^S\hat{x}_7^S) & \\
\dot{x}_3^S &= \alpha_{11}x_1^S\hat{x}_2^S - \beta_{11}x_2^S & - \gamma_{11}^S\hat{x}_1^S & - Cx_3^S & + \delta_{11}x_4^S\hat{x}_5^S & + \rho_{11}(\hat{x}_5^S\hat{x}_7^S + \hat{x}_6^S\hat{x}_8^S) & \\
\dot{x}_4^S &= & \gamma_{12}^{*S}\hat{x}_6^S & - C(x_4^S - x_4^{*S}) & + \epsilon_1(\hat{x}_2^S\hat{x}_6^S - \hat{x}_3^S\hat{x}_5^S) & + \epsilon_2(\hat{x}_7^S\hat{x}_{10}^S - \hat{x}_8^S\hat{x}_9^S) & \\
\dot{x}_5^S &= -\alpha_{12}x_1^S\hat{x}_6^S - \beta_{12}x_6^S & & - Cx_5^S & - \delta_{12}\hat{x}_3^S x_4^S & + \rho_{12}(\hat{x}_2^S\hat{x}_8^S - \hat{x}_3^S\hat{x}_7^S) & + \gamma_{12}'^S\hat{x}_8^S \\
\dot{x}_6^S &= \alpha_{12}x_1^S\hat{x}_5^S - \beta_{12}x_5^S & - \gamma_{12}^S x_4^S & - Cx_6^S & + \delta_{12}\hat{x}_2^S x_4^S & - \rho_{12}(\hat{x}_2^S\hat{x}_7^S + \hat{x}_3^S\hat{x}_8^S) & - \gamma_{12}'^S\hat{x}_7^S \\
\dot{x}_7^S &= -\alpha_{21}x_1^S\hat{x}_8^S - \beta_{21}x_8^S & & - Cx_7^S & - \delta_{21}x_4^S\hat{x}_{10}^S & - \rho_{21}(\hat{x}_2^S\hat{x}_6^S + \hat{x}_3^S\hat{x}_5^S) & + \gamma_{21}'^S\hat{x}_6^S \\
\dot{x}_8^S &= \alpha_{21}x_1^S\hat{x}_7^S - \beta_{21}x_7^S & & - Cx_8^S & + \delta_{21}x_4^S\hat{x}_9^S & + \rho_{21}(\hat{x}_2^S\hat{x}_5^S - \hat{x}_3^S\hat{x}_6^S) & - \gamma_{21}'^S\hat{x}_5^S \\
\dot{x}_9^S &= -\alpha_{22}x_1^S\hat{x}_{10}^S - \beta_{22}x_{10}^S & & - Cx_9^S & - \delta_{22}x_4^S\hat{x}_8^S & & \\
\dot{x}_{10}^S &= \alpha_{22}x_1^S\hat{x}_9^S - \beta_{22}x_9^S & & - Cx_{10}^S & + \delta_{22}x_4^S\hat{x}_7^S & &
\end{aligned}
$$

$$\dot{y}_2 = \omega_2 y_3 - Cy_2 + \frac{T\omega_2}{\lambda_2}\frac{1}{2\pi^2 b}\sum_k c_{3k}(\hat{x}_k^N - \hat{x}_k^S)$$

$$\dot{y}_3 = -\omega_2 y_2 - Cy_3 - \frac{T\omega_2}{\lambda_2}\frac{1}{2\pi^2 b}\sum_k c_{2k}(\hat{x}_k^N - \hat{x}_k^S)$$

$$\dot{y}_5 = \omega_5 y_6 - Cy_5 + \frac{T\omega_5}{\lambda_5}\frac{1}{2\pi^2 b}\sum_k c_{6k}(\hat{x}_k^N - \hat{x}_k^S)$$

$$\dot{y}_6 = -\omega_5 y_5 - Cy_6 - \frac{T\omega_5}{\lambda_5}\frac{1}{2\pi^2 b}\sum_k c_{5k}(\hat{x}_k^N - \hat{x}_k^S)$$

$$\dot{y}_7 = \omega_7 y_8 - Cy_7 + \frac{T\omega_7}{\lambda_7}\frac{1}{2\pi^2 b}\sum_k c_{8k}(\hat{x}_k^N - \hat{x}_k^S)$$

$$\dot{y}_8 = -\omega_7 y_7 - Cy_8 - \frac{T\omega_7}{\lambda_7}\frac{1}{2\pi^2 b}\sum_k c_{7k}(\hat{x}_k^N - \hat{x}_k^S)$$

$$\dot{y}_9 = \omega_9 y_{10} - Cy_9 + \frac{T\omega_9}{\lambda_9}\frac{1}{2\pi^2 b}\sum_k c_{10k}(\hat{x}_k^N - \hat{x}_k^S)$$

$$\dot{y}_{10} = -\omega_9 y_9 - Cy_{10} - \frac{T\omega_9}{\lambda_9}\frac{1}{2\pi^2 b}\sum_k c_{9k}(\hat{x}_k^N - \hat{x}_k^S)$$

$$\Psi^N = \sum_{i=1}^{N} \hat{x}_i^N(t)\Upsilon_i^N, \quad \hat{x}_i^N \equiv x_i^N + y_i, \tag{34a}$$

$$\Psi^S = \sum_{i=1}^{N} \hat{x}_i^S(t)\Upsilon_i^S, \quad \hat{x}_i^S \equiv x_i^S - y_i. \tag{34b}$$

The boundary forcing (17) is seen to be $D(x) = T\Sigma_k \Upsilon_k^{\uparrow}(x,0)(\hat{x}_k^N - \hat{x}_k^S)$ at the longitudes of the ducts, where we have defined northward- and southward-propagating parts for the real modes Υ_k, which are linear combinations of the Φ_j, using Eq. (19) [e.g., $\Upsilon_3^{\uparrow}(x,0) = b\cos x = \frac{1}{2}\Upsilon_2(x,0)$, $\Upsilon_5^{\uparrow}(x,0) = -b\sin x = -\frac{1}{2}\Upsilon_6(x,0)$] and have noted $\Upsilon_k^{\uparrow}(x,0)$

TABLE IV. The coupling coefficients for the two-hemisphere system in Table III, in terms of overlap integrals that depend on the sizes and relative positions of the ducts in Fig. 4. (Coordinates are chosen so that $\int_{x\in\text{ducts}}\cos 2x\,dx=0$.)

$c_{1k}=c_{i1}=c_{4k}=c_{i4}$	$=0$	
$c_{23}=-c_{32}=c_{26}=-c_{35}$	$=\frac{2}{b}I_A$	$I_A\equiv\frac{1}{2}\int_{x\in\text{ducts}}dx$
$c_{78}=c_{7,10}$	$=\frac{2}{b}(I_A+I_{A'})$	
$-c_{87}=-c_{89}$	$=\frac{2}{b}(I_A-I_{A'})$	$I_{A'}\equiv\frac{1}{2}\int_{x\in\text{ducts}}\cos 4x\,dx$
$c_{22}=c_{25}=-c_{36}=-c_{33}$	$=\frac{2}{b}I_B$	
$c_{28}=c_{2,10}=c_{73}=c_{76}$	$=\frac{2}{b}I_C$	$I_B\equiv-\int_{x\in\text{ducts}}\cos x\sin x\,dx$
$c_{27}=c_{29}=-c_{83}=-c_{86}$	$=\frac{2}{b}I_D$	
$-c_{38}=-c_{3,10}=c_{72}=c_{75}$	$=\frac{2}{b}I_E$	$I_C\equiv\int_{x\in\text{ducts}}\cos x\cos 2x\,dx$
$c_{37}=c_{39}=c_{82}=c_{85}$	$=\frac{2}{b}I_F$	
$c_{77}=-c_{8,10}=c_{79}=-c_{88}$	$=\frac{2}{b}I_G$	$I_D\equiv-\int_{x\in\text{ducts}}\cos x\sin 2x\,dx$
$c_{56}=-c_{65}=c_{53}=-c_{62}$	$=\frac{4}{b}I_A$	
$c_{9,10}=c_{98}$	$=\frac{4}{b}(I_A+I_{A'})$	$I_E\equiv-\int_{x\in\text{ducts}}\sin x\cos 2x\,dx$
$-c_{10,9}=-c_{10,7}$	$=\frac{4}{b}(I_A-I_{A'})$	
$-c_{63}=c_{55}=c_{52}=-c_{66}$	$=\frac{4}{b}I_B$	$I_F\equiv-\int_{x\in\text{ducts}}\sin x\sin 2x\,dx$
$c_{58}=c_{5,10}=c_{96}=c_{93}$	$=\frac{4}{b}I_C$	
$c_{57}=c_{59}=-c_{10,3}=-c_{10,6}$	$=\frac{4}{b}I_D$	$I_G\equiv-\int_{x\in\text{ducts}}\sin 2x\cos 2x\,dx$
$-c_{68}=-c_{6,10}=c_{95}=c_{92}$	$=\frac{4}{b}I_E$	
$c_{67}=c_{69}=c_{10,5}=c_{10,2}$	$=\frac{4}{b}I_F$	
$-c_{10,8}=c_{99}=-c_{10,10}=c_{97}$	$=\frac{4}{b}I_G$	

$=-\Upsilon_k^{\downarrow}(x,0)$. The coefficients of the modes in Ψ_B are then found from Eqs. (23) and (30):

$$\zeta_j(t)=\int_{-\infty}^{t}e^{(-i\omega_j-C)(t-t_0)}\frac{1}{2\pi^2 b}\sum_k\int_{x\in\text{ducts}}\left(\frac{\partial}{\partial y}\overline{\Phi}_j(x,0)\right)\times\Upsilon_k^{\uparrow}(x,0)\frac{-i\omega_j T[\hat{x}_k^N(t_0)-\hat{x}_k^S(t_0)]}{\lambda_j}dx\,dt_0 \tag{35}$$

or, differentiating,

$$\dot{\zeta}_j=(-i\omega_j-C)\zeta_j-i\omega_j\frac{T}{2\pi^2 b}\sum_{k=1}^{N}w_{jk}(\hat{x}_k^N-\hat{x}_k^S)/\lambda_j, \tag{36}$$

where we have introduced notation for the overlap integrals:

$$w_{jk}\equiv\int_{x\in\text{ducts}}\left(\frac{\partial}{\partial y}\overline{\Phi}_j(x,0)\right)\Upsilon_k^{\uparrow}(x,0)dx. \tag{37}$$

From Eqs. (27) and (4) it is apparent that first-order differential equations for the coefficients of the modes in the coupled model can be obtained by substituting $\hat{x}_i$ for x_i in all terms of the single-hemisphere equations except the time-derivative, β-effect, and dissipation ($\sim C$) terms, then including equations for $\dot{y}_i$ that can be obtained from the real and imaginary parts of Eq. (36), according to the definitions in Eqs. (33b), (31), (7), and Table II. The equations for $\dot{y}_i$ can be expressed in terms of the coefficients

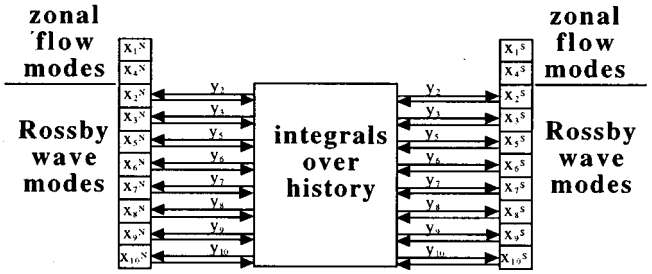

FIG. 5. Schematic representation of the stucture of the truncated 28-component model of the coupled hemispheres. Zonal flow modes are uncoupled, while each Rossby mode is coupled to all Rossby modes in the opposite hemisphere at all past times.

$$c_{ik} \equiv \frac{1}{b^2} \int_{x \in \text{ducts}} \left(\frac{\partial}{\partial y} \Upsilon_i(x,0) \right) \Upsilon_k^{\uparrow}(x,0)\, dx, \qquad (38)$$

which are analogous to the w_{jk}. For the coupled system corresponding to the 10-component single-hemisphere de Swart system ($N=10$), the resulting 28-variable system is specified in Table III. There are 10 variables for each hemisphere as before, plus 8 for the coefficents of the coupling modes, since for the zonal flow modes $y_1=y_4=0$, whence also $\hat{x}_1=x_1$, $\hat{x}_4=x_4$. The coupling coefficients c_{ik} are expressed in terms of eight independent quantities, given by overlap integrals that depend formally on the sizes and relative positions of the ducts, in Table IV.

The key approximation that enables the formulation of our coupled model is that the state of the whole system can be expanded in the tensor product basis $\{\Phi_m^N \otimes \Phi_n^S\}_{m,n=1}^{\infty}$ composed of the modes of the two separate mid-latitude systems. This assumption would clearly be false if, for instance, the westerly ducts spanned the entire equator. In that case, even modes (in y) of the whole system, corresponding to half-integer values of j_2 with a phase shift, which satisfied the boundary conditions (6) only at $y=\pi b$ and $y=-\pi b$, would have to be considered (if the forcing terms were similarly generalized). But such modes could not be expanded in the tensor product basis. A heuristic argument for the sufficiency of our approximation with a realistic configuration of westerly ducts, on the other hand, is then the following: considering solutions of the dynamical equation in the entire two-hemisphere region except for the easterly barriers, the stream function might contain an even component at the longitudes of the ducts that would vanish at the longitudes of the barriers. But it would require a summation to higher order in the *zonal* wave number than we have considered to patch these two parts of the solution together, for ducts that are $\approx 45°$ wide. So to the extent that the low-order models [22,12] adequately describe single-hemisphere dynamics, the tensor product approximation should describe the coupled system.

The form of the coupling in Table III is similar to that of a control signal that vanishes when the two systems are synchronized, as in [2], [3], and [19]. But in the model described here the y_i's involve a time integral (35) that depends on prior states of the system at the tropical boundary. The structure of the model, as schematized in Fig. 5, is similar to that of the generalized Pecora-Carroll [1] configuration of Lorenz

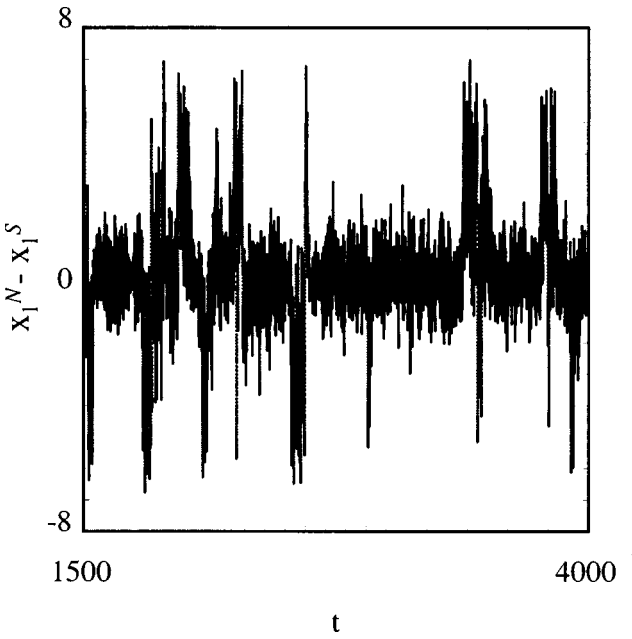

FIG. 6. The difference between the simultaneous states of the two hemispheres as given by $x_1^N - x_1^S$ vs t for an adaptive Runge-Kutta numerical integration of the 28-component coupled system specified in Table III with transmission coefficient $T=0.95$, and with the coupling coefficients c_{ik} given by $I_A=0.8$, $I_{A'}=0$, $I_B=0.25$, $I_C=0.47$, $I_D=-0.47$, $I_E=-0.23$, $I_F=-0.23$, and $I_G=-0.25$. ($I_{A'}=0$ is equivalent to approximating coefficients coupling modes with the same zonal structure by their average values for given total width of ducts.) Other parameters are as in Fig. 2.

systems described in Sec. II. The zonal flow modes play the role of the uncoupled variables that appeared in these earlier models and that are especially significant in the Pecora-Carroll configuration [1]. [Specifically, the variable S in Eq. (1c) plays a role analogous to that of the y_i's in the equations in Table III, while the expressions $(X-S)$ and (X_1+S) in the two subsystems (1a–1c) and (1e–1f), are analogous to the $\hat{x}_i^N$'s and $\hat{x}_i^S$'s, respectively.] The central question is whether partial synchronization, as described in Sec. II, is also possible in an intermediate model such as that of Table III.

V. RESULTS AND INTERPRETATION

The difference between the corresponding variables x_1^N and x_1^S, for a typical numerical integration of the 28-variable coupled system is shown in Fig. 6. Because of the idealizations in the shape and transmission properties of the ducts depicted in Fig. 4, and because the ''ducts'' that transmit different modes are differently shifted longitudinally, according to the Doppler-shift analysis in Sec. III B, we did not compute coefficients for a specific configuration of ducts but simply chose values of the overlap integrals in Table IV that are typical for ducts totaling 90° in width.

It is apparent that the two subsystems do not synchronize, even intermittently. We therefore assess the possibility that some correlation between the gross states of the two subsystems may still be discerned. Since the single-hemisphere system lends itself to a description in terms of regimes [12],

TABLE V. Joint probability matrices as in Table I, but for the trajectory depicted in Fig. 6 of the coupled meteorological systems specified in Table III, where the regimes are zonal flow and blocked flow, defined by $x_1>3$ and $x_1<3$, respectively, in either hemisphere.

	(a) P		(b) P^{ind}	
	N zonal	N blocked	N zonal	N blocked
S zonal	0.67	0.11	0.65	0.14
S blocked	0.15	0.06	0.18	0.04
		$\mathcal{C}=0.16$		

we compute the joint probabilities of the simultaneous residence of the two subsystems in given pairs of regimes, as we did for the coupled Lorenz systems in Sec. II. Absent a rigorous definition of ''regime,'' but given the apparent regime structure of the trajectory in Fig. 2, we call subsystem N (S) *zonal* at any time t if $x_1^N(t)>3$ [$x_1^S(t)>3$]. Otherwise we call subsystem N (S) *blocked* at time t. (The separate identity of the seldom-occupied ''transitional'' regime described in [12] is ignored here.) The joint probabilites $P_{i,j}$, and the corresponding probability values $P_{i,j}^{\text{ind}}$ in the case where the two subsystems individually have the same statistics but are assumed independent, are given in Table V.

The diagonal elements of the matrix P are larger than

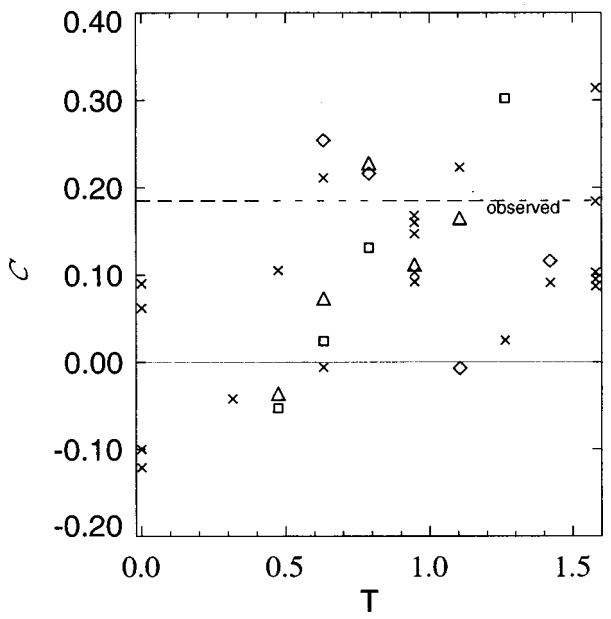

FIG. 7. The interhemispheric regime correlation $\mathcal{C}$ (39), which quantifies the tendency for blocked states to co-occur, for varying interhemispheric transmission coefficient T, as defined in Eq. (17), for integrations of the model defined in Table III with different randomly chosen initial conditions. Crosses denote correlation values for integrations with other parameters as in Fig. 6. Squares are for $I_A=1.2$, $I_{A'}=0$, $I_B=0.18$, $I_C=0.4$, $I_D=-0.4$, $I_E=-0.5$, $I_F=0.5$, and $I_G=-0.125$. Diamonds for $I_A=1.2$, $I_{A'}=0.3$, $I_B=0.18$, $I_C=0.4$, $I_D=-0.4$, $I_E=-0.5$, $I_F=-0.5$, and $I_G=-0.125$. Triangles are for runs with different topographic parameters in the two hemispheres: $\gamma^N=1.2$, $\gamma^S=0.85$ and other parameters as in Fig. 6. The dotted line is $\mathcal{C}$ for observed data [29].

TABLE VI. Joint probability matrices as in Table V, but for an integration with a smaller topography parameter in the southern hemisphere: $\gamma^S=0.85$, than in the northern hemisphere $\gamma^N=1.2$ ($T=1.11$ and other parameters are as in Table V).

	(a) P		(b) P^{ind}	
	N zonal	N blocked	N zonal	N blocked
S zonal	0.51	0.34	0.48	0.37
S blocked	0.05	0.09	0.08	0.07
		$\mathcal{C}=0.17$		

those of the matrix P^{ind}, while the off-diagonal elements are smaller. This indicates correlation. Letting

$$\mathcal{C}\equiv\frac{P_{bb}-P_{bb}^{\text{ind}}}{\sqrt{\sum_{r=z,b}P_{z,r}\sum_{r=z,b}P_{b,r}\sum_{s=z,b}P_{s,z}\sum_{s=z,b}P_{s,b}}} \tag{39}$$

be the standard measure of this correlation, we plot $\mathcal{C}$ as a function of the transmission coefficient T in Fig. 7. While $T=1$ in Fig. 7 corresponds to a naive assumption about the nature of the ducts, corresponding to the illustration in Fig. 4, and one might expect smaller values of T in the realistic case that Rossby waves are attenuated, there is also evidence that realistically shaped ducts might serve to focus Rossby waves [28], possibly giving an effective $T>1$. The scatter of the data points in Fig. 7 at the higher values of T for which several integrations were conducted demonstrate the correlations in this numerical experiment to be significant.

Results for numerical integrations with two alternative configurations of somewhat larger ducts are also shown in Fig. 7. The correlations are little affected. The effects of asymmetry between the hemispheres can be assessed in a realistic context by choosing different topographic parameters, $\gamma^S\neq\gamma^N$, for the two hemispheres, in the system of equations in Table III. Though the resulting joint probabilities listed in Table VI show less blocking in the southern hemisphere and more blocking in the northern hemisphere as compared to the case analyzed in Table V, for example, the value of the correlation (also plotted in Fig. 7) shows that a physically significant degree of asymmetry can be tolerated.

To interpret the regime correlation results in the absence of clear synchronization in any portion of the trajectories, we ask how far the system is from a synchronized state as a function of time. The Euclidean distance between the states of the two subsystems is defined as it was for the coupled Lorenz systems in Sec. II. In the meteorological case, this distance is

$$D(t)=\sqrt{\sum_{i=1}^{10}(\hat{x}_i^N-\hat{x}_i^S)^2}=\sqrt{\sum_{i=1}^{10}(x_i^N-x_i^S+2y_i)^2}, \tag{40}$$

which corresponds to an $L2$ norm on the space of stream functions. $D(t)$ vanishes if and only if the system is in a state which is and will remain synchronized. Such states form the dynamically invariant synchronization manifold. $D(t)/\sqrt{2}$

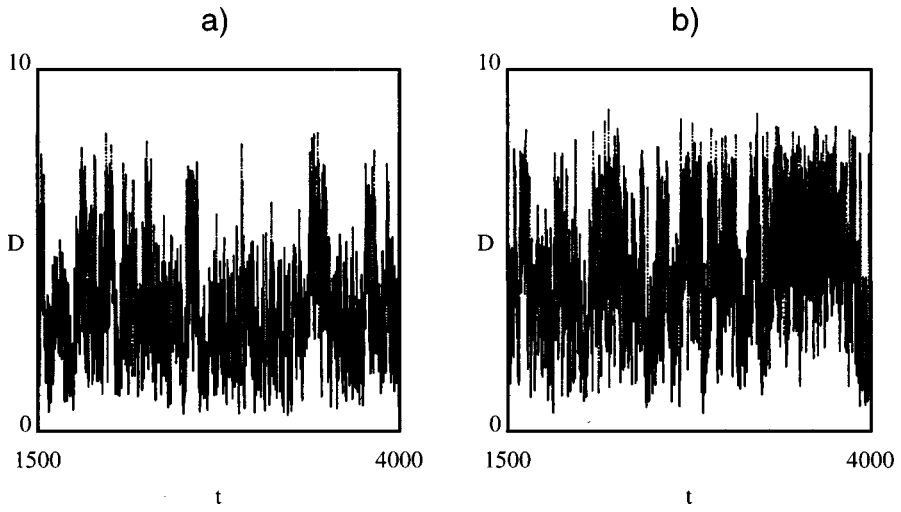

FIG. 8. The distance D between the states of the two hemispheres [defined in Eq. (40)] vs time, for (a) the trajectory of the coupled system represented in Fig. 6 and (b) a trajectory of the same system with the coupling turned off ($T=0$ in the equations in Table III).

gives the distance from this manifold. $D(t)$ is plotted in Fig. 8, for the trajectory of the coupled system shown in Fig. 6, and for the same system with the coupling turned off ($T=0$). Histograms of D values for the two trajectories are displayed in Fig. 9. It is seen that the coupled system generally spends more time near the synchronization manifold. This is attributable to effects in all parts of phase space—even portions of the trajectory far from synchronization are drawn in.

To inquire as to whether the correlations in the 28-component meteorological system are of the same dynamical origin as the correlations in the time-lagged-coupled Lorenz systems, one might naively scale the coupling matrix defined by the equations in Table III to uncover on-off intermittency. Scaling all the coefficients c_{ij} was found to be ineffective, however, apparently because the fast-time-scale fixed points given approximately by $y_i=(x_i^S-x_i^N)/2$ (or equivalently $\hat{x}_i^N=\hat{x}_i^S$) are unstable or have inadequate basins of attraction in the system defined by the scaled coefficients. A system defined by scaling just some of the coefficients c_{ij}, on the other hand, has the same fixed points, but possibly with better stability properties, making the equations in Table III more efficacious in achieving the quasi-steady-state values of the y_i. Manifestly on-off intermittent behavior in fact appears in the trajectory in Fig. 10 for a system defined by scaling only those coefficients that couple corresponding modes in the two hemispheres. The magnified values are larger than can be realized with any configuration of ducts in the model and can instead be interpreted as due to a decrease in the time scale associated with the coupling. But the effect of the scaling is also to increase the relative magnitudes of select coupling coefficients as compared to others.

The loss of periods of exact synchronization in the case of physical parameter values is therefore due both to finite sig-

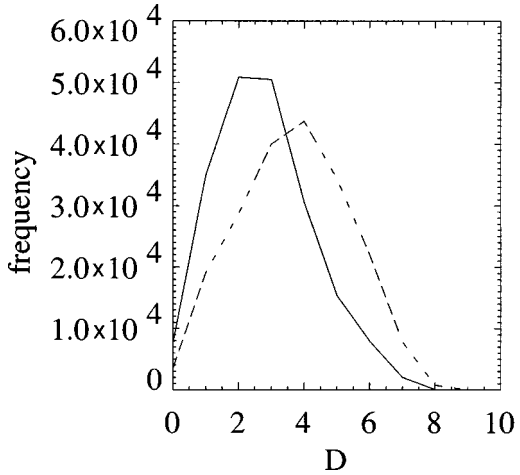

FIG. 9. Histograms of D for the two plots shown in Fig. 8. The solid line is for the coupled case [Fig. 8(a)]; the dashed line is for the uncoupled case [Fig. 8(b)]. The frequencies are the numbers of time steps spent in bins of size $\Delta D=1$ in the respective numerical integrations.

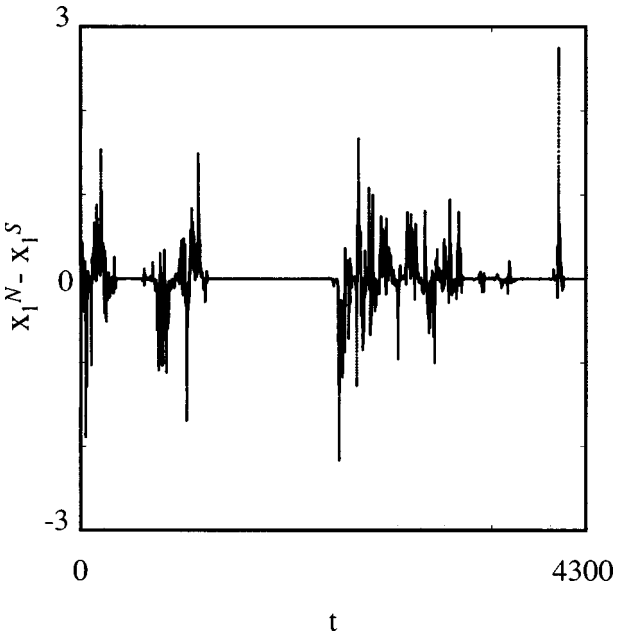

FIG. 10. A trajectory of the coupled-hemisphere system depicted by $x_1^N-x_1^S$ vs t as in Fig. 6 but with the coupling coefficients $c_{23}, c_{32}, c_{56}, c_{65}, c_{78}, c_{87}, c_{9,10}$, and $c_{10,9}$ increased by a factor of 38. (These are the diagonal coupling coefficients in the equations for the $\dot{y}_i$ in Table III.) Other coefficients are as in Fig. 6.

TABLE VII. Relative frequencies of co-occurrence of regime pairs in observed meteorological data (NCEP data [29]) for the period 1979–95, expressed as joint probabilities as in Table V.

	(a) P		(b) P^{ind}	
	N zonal	N blocked	N zonal	N blocked
S zonal	0.33	0.41	0.31	0.43
S blocked	0.09	0.17	0.11	0.15
		$\mathcal{C}=0.09$		

nal propagation speed and to the particular set of mode cross couplings in a realistic setting. One might therefore be concerned as to whether the partial synchronization behavior would be preserved as the number of modes is increased, since the number of troublesome coupling terms increases faster than the number of effective couplings. However, this effect is offset by a decrease in the size of the nondiagonal coefficients for higher modes, due to the decreasing values of the overlap integrals in the ducts for modes with differing zonal wave number, and by a decrease in the factors ω_j in the equations for the coupling variables, since according to Eq. (8), $\omega_{j_1 j_2}$ varies inversely as the zonal wave number j_1 and as the inverse square of the meridional wave number j_2. Furthermore, the synchronization tendency is expected to be enhanced by the inclusion of meridionally even modes of the two-hemisphere system regarded as a whole, which will be required in a higher-order truncation for the reasons discussed near the end of Sec. IV. Therefore the correlations observed in the low-order model may be preserved.

VI. COMPARISON WITH OBSERVATIONS

While a complete discussion of observational evidence for co-occurrence of blocked states in opposite hemispheres will be given elsewhere, here we summarize the relevant meteorological data. Using a standard meteorological diagnostic, described in Appendix B, for blocking at 60° N latitude (any longitude) and 40° S latitude (any longitude), we have computed the relative frequencies of co-occurence of the possible regime pairs for the period 1979–1995, in data at 6-h increments obtained from the National Centers for Environmental Prediction (NCEP) [29]. Results are presented in Table VII, in the same form as the joint probabilities of regime co-occurrence for the low-order model. Blocking events are seen to co-occur to a small degree. Additional confirmation of the synchronized chaos theory can be obtained by restricting the statistics to the months December, January, and February, since it is generally only during these months when the westerly ducts are open, as seen in Fig. 11, and only then is interhemispheric coupling possible. (An alternative explanation of the co-occurrence statistics is that there is a common causative factor in the tropics, associated with the westerly ducts, which induces blocking in either hemisphere, as might be inferred from [30], for example. Further work is needed to clarify the implications of the data.) The correlation $\mathcal{C}$ for these winter statistics, analyzed in Table VIII, is indeed higher than the correlation for the full-year statistics in Table VII. The statistical significance of these results is implied by the error bars on $\mathcal{C}$ in Table VIII,

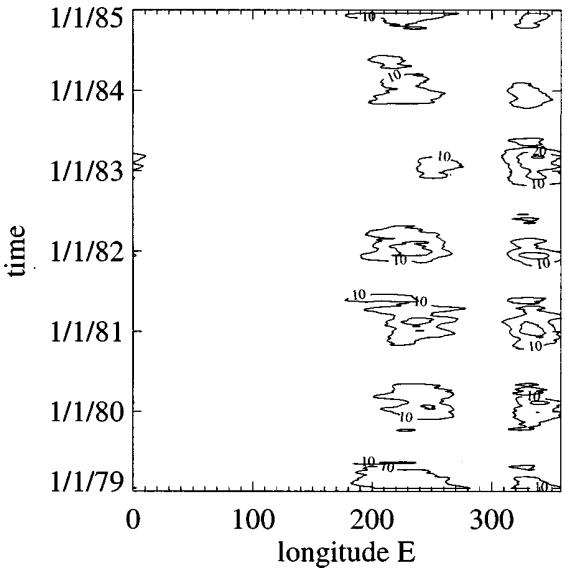

FIG. 11. Contour plot of the zonal component of the upper-tropospheric (200 mbar) tropical wind u (in m/s), which defines the westerly ducts, vs longitude and time. The tropical wind is defined as the average of the wind between 10° N and 10° S, also averaged over 30 days. Only positive (westerly) values of the wind are shown.

which were derived by partitioning the 16-y data set into five segments and computing the standard error of the mean.

It is noteworthy that blocking events at 60° N correlate with events at 40° S, breaking the naively expected symmetry. This is apparently the result of topographic asymmetry due to the different distribution of the land masses in the southern hemisphere in the direction of the equator. The observed correlations can be viewed as an extension of the phenomenon of generalized synchronization, observed in asymmetric low-order systems [4], to the context of a continuous medium.

Analysis of weather phenomena in terms of correlations between data at remote points on the globe is not new to meteorology. In 1924, Walker [31] first postulated the existence of a web of such relationships in his unsuccessful attempt to find predictors for the strength of the Indian monsoon. Later, Bjerknes [32] coined the term *teleconnection* in reference to the now well-known relationships between El Nino and global weather phenomena. Systematic studies [33] subsequently identified a number of teleconnection patterns that are quite useful in describing the variability of the atmospheric circulation. Observed correlations are thought to be

TABLE VIII. Relative frequencies of co-occurrence of regime pairs in the period 1979–95 as in Table VII, but for the months December, January, and February only. (Error bars on $\mathcal{C}$ were computed as the standard error of the mean in a partitioned data set.)

	(a) P		(b) P^{ind}	
	N zonal	N blocked	N zonal	N blocked
S zonal	0.16	0.16	0.12	0.20
S blocked	0.21	0.47	0.25	0.43
		$\mathcal{C}=0.18\pm0.08$		

mediated by the exchange of Rossby waves [26] between teleconnected subsystems. But in general, each of these subsystems evolves according to its own intrinsically chaotic dynamics. The results of the previous section demonstrate that the Rossby-wave-mediated correlations are consistent with the chaotic subsystem dynamics and that the two behaviors can be captured in a low-order bidirectionally coupled model.

VII. SUMMARY AND CONCLUSIONS

We have shown that a form of partially synchronized chaos can occur in a pair of adjacent bidirectionally coupled extended systems, with spatial separation between corresponding degrees of freedom, in a spectrally truncated theoretical model. We have presented preliminary evidence that these results may approximate physical behavior in the Earth's atmosphere. In particular, the time lags introduced by the spatial separation do not destroy all trace of synchronous behavior.

In regard to the robustness of this behavior, we have shown that it is preserved in the presence of significant asymmetry between the two systems. While we have not directly addressed the issue of noise, results obtained by others [5] for synchronization of low-order systems in the presence of noise should apply to our low-order representations of continuous systems as well. Indeed, the high-order modes that were omitted through our truncation, and that have not been thought to affect the qualitative large-scale dynamics of either hemisphere separately, are also not expected to cause greater degradation of the synchronous behavior than would an equal amount of uncorrelated noise. We also have not addressed the issue of variations in the coupling channel, as would be due to periodic closure of the westerly ducts, for instance, but recent findings on the possibility of synchronization with only occasional coupling [34] are encouraging.

Partial synchronization occurs in our model because of the attractive properties of a synchronization manifold in the coupled system. Though this manifold is unstable, its presence affects the global dynamics of the system. It is not the case, for instance, that trajectories are affected only when they are near synchronization, as compared to the case of no coupling. While we have shown by example that such behavior can result from the extension of on-off intermittency to regions of parameter space far from the blowout bifurcation point, a thorough description of this behavior, which is on-off intermittent in name only, is still desired.

The analysis presented here has been possible because of the fortuitous circumstance that the two coupled systems are semiautonomous. One would hope that partially synchronized chaos might be observed in a fluid system where there is no analog of the belt of tropical easterlies nearly separating the hemispheres. A theory of laminar regions in a turbulent fluid (indeed the segments of on-off intermittent trajectories very near the invariant manifold are often called the ''laminar phase,'' e.g., [17]), or of coherent structures in turbulence generally, would be such an application. Unfortunately, the methods of this paper do not lend themselves to the case of fully coupled subsystems. Whether and how low-order chaotic synchronization can be applied to general turbulence remain open questions.

Nevertheless, complex systems in nature often give way to decomposition into loosely coupled subsystems. It has been suggested [35] that the utility of the concept of low-dimensional chaos in the Earth's atmosphere, for instance, is in describing such subsystems, rather than weather as a whole. When such subsystems are identical or similar, then there is the possibility of partially synchronized chaos. In some cases this may take the form of recognizable on-off intermittency. In others, more subtle correlations may still be discerned, since it has been shown that this is not precluded by the finite spatial extent of the subsystems.

ACKNOWLEDGMENTS

This work was performed under National Science Foundation Grants NSF-ATM-9526030 and NSF-ATM-9312760. The author wishes to thank Professor Peter Webster for suggesting the configuration of atmospheric systems that was analyzed in this paper as a possible example of synchronized chaos, and Professor Jeffrey Weiss for many useful discussions. He also thanks Dr. Antonello Provenzale for editorial comments.

APPENDIX A: BOUNDARY GREEN'S FUNCTION FOR THE LINEAR VORTICITY EQUATION ON A β PLANE

To construct a boundary Green's function that can be used to generate a solution to the linear vorticity equation, with inhomogeneous boundary conditions, via Eq. (23), we follow the methods of [27]. It is useful to first establish the reciprocity relation:

$$G_\beta(\mathbf{r},t|\mathbf{r}_0,t_0)=G_{-\beta}(\mathbf{r}_0,-t|\mathbf{r},-t_0) \tag{A1}$$

for the (ordinary) Green's function G_β satisfying Eq. (24) with homogeneous boundary conditions, on the ''β plane'' $f=\beta y$.

The proof of Eq. (A1) is as follows: consider the two equations

$$\frac{1}{C}\frac{\partial}{\partial t}\nabla^2 G_\beta(\mathbf{r},t|\mathbf{r}_0,t_0)+\frac{\beta}{C}\frac{\partial}{\partial x}G_\beta(\mathbf{r},t|\mathbf{r}_0,t_0)+\nabla^2 G_\beta(\mathbf{r},t|\mathbf{r}_0,t_0)=\delta^2(\mathbf{r}-\mathbf{r}_0)\,\delta(t-t_0)$$

$$-\frac{1}{C}\frac{\partial}{\partial t}\nabla^2 G_{-\beta}(\mathbf{r},-t|\mathbf{r}_1,-t_1)-\frac{\beta}{C}\frac{\partial}{\partial x}G_{-\beta}(\mathbf{r},-t|\mathbf{r}_1,-t_1)+\nabla^2 G_{-\beta}(\mathbf{r},-t|\mathbf{r}_1,-t_1)=\delta^2(\mathbf{r}-\mathbf{r}_1)\,\delta(t-t_1),$$

which follow from Eq. (23). Multiply the first equation by $G_{-\beta}(\mathbf{r},-t|\mathbf{r}_1,-t_1)$ and the second by $G_\beta(\mathbf{r},t|\mathbf{r}_0,t_0)$, subtract, and integrate over the region of interest (northern hemisphere) and over t from $-\infty$ to t_0^+, to obtain

$$\frac{1}{C}\int_{-\infty}^{t_0^+} dt \int dxdy\left(G_{-\beta}(\mathbf{r},-t|\mathbf{r}_1,-t_1)\frac{\partial}{\partial t}\nabla^2 G_\beta(\mathbf{r},t|\mathbf{r}_0,t_0)+G_\beta(\mathbf{r},t|\mathbf{r}_0,t_0)\frac{\partial}{\partial t}\nabla^2 G_{-\beta}(\mathbf{r},-t|\mathbf{r}_1,-t_1)\right)$$
$$+\frac{\beta}{C}\int_{-\infty}^{t_0^+} dt \int dxdy\left(G_{-\beta}(\mathbf{r},-t|\mathbf{r}_1,-t_1)\frac{\partial}{\partial x} G_\beta(\mathbf{r},t|\mathbf{r}_0,t_0)+G_\beta(\mathbf{r},t|\mathbf{r}_0,t_0)\frac{\partial}{\partial x} G_{-\beta}(\mathbf{r},-t|\mathbf{r}_1,-t_1)\right)$$
$$+\int_{-\infty}^{t_0^+} dt \int dxdy[G_{-\beta}(\mathbf{r},-t|\mathbf{r}_1,-t_1)\nabla^2 G_\beta(\mathbf{r},t|\mathbf{r}_0,t_0)-G_\beta(\mathbf{r},t|\mathbf{r}_0,t_0)\nabla^2 G_{-\beta}(\mathbf{r},-t|\mathbf{r}_1,-t_1)]$$
$$=G_{-\beta}(\mathbf{r}_0,-t_0|\mathbf{r}_1,-t_1)-G_\beta(\mathbf{r}_1,t_1|\mathbf{r}_0,t_0). \tag{A2}$$

We shall show that the left-hand side of Eq. (A2) vanishes. The first integral in Eq. (A2) can be simplified by integrating the second term in the integrand by parts in the temporal dimension, yielding

$$\int_{-\infty}^{t_0^+} dt \int dxdy\left(G_{-\beta}(\mathbf{r},-t|\mathbf{r}_1,-t_1)\frac{\partial}{\partial t}\nabla^2 G_\beta(\mathbf{r},t|\mathbf{r}_0,t_0)+G_\beta(\mathbf{r},t|\mathbf{r}_0,t_0)\frac{\partial}{\partial t}\nabla^2 G_{-\beta}(\mathbf{r},-t|\mathbf{r}_1,-t_1)\right)$$
$$=\int_{-\infty}^{t_0^+} dt \int dxdy\left(G_{-\beta}(\mathbf{r},-t|\mathbf{r}_1,-t_1)\frac{\partial}{\partial t}\nabla^2 G_\beta(\mathbf{r},t|\mathbf{r}_0,t_0)-\frac{\partial}{\partial t}[G_\beta(\mathbf{r},t|\mathbf{r}_0,t_0)]\nabla^2 G_{-\beta}(\mathbf{r},-t|\mathbf{r}_1,-t_1)\right)$$
$$+\int dxdy[G_\beta(\mathbf{r},t|\mathbf{r}_0,t_0)\nabla^2 G_{-\beta}(\mathbf{r},-t|\mathbf{r}_1,-t_1)]_{t=-\infty}^{t=t_0^+}. \tag{A3}$$

Considering the last integral in Eq. (A3), the second factor in the integrand vanishes at the lower limit because of the causal boundary condition on G, while the first factor vanishes at the upper limit for the same reason (assuming, without loss of generality, that $t_1<t_0$). The first integral on the right hand side of Eq. (A3) can be evaluated with the aid of Green's theorem in two dimensions:

$$\int [U\nabla^2 V-V\nabla^2 U]d\mathbf{A}=\oint [U\vec{\nabla}V-V\vec{\nabla}U]\cdot\vec{\mathbf{n}}ds, \tag{A4}$$

where U and V are any scalar fields and $\vec{\mathbf{n}}$ is the outward-pointing unit normal along the boundary of the two-dimensional (2D) domain. Letting $U=G_{-\beta}(\mathbf{r},-t|\mathbf{r}_1,-t_1)$ and $V=(\partial/\partial t)G_\beta(\mathbf{r},t|\mathbf{r}_0,t_0)$, we find

$$\int_{-\infty}^{t_0^+} dt \int dxdy\left[G_{-\beta}(\mathbf{r},-t|\mathbf{r}_1,-t_1)\frac{\partial}{\partial t}\nabla^2 G_\beta(\mathbf{r},t|\mathbf{r}_0,t_0)+G_\beta(\mathbf{r},t|\mathbf{r}_0,t_0)\frac{\partial}{\partial t}\nabla^2 G_{-\beta}(\mathbf{r},-t|\mathbf{r}_1,-t_1)\right]$$
$$=\int_{-\infty}^{t_0^+} dt \oint \left(G_{-\beta}(\mathbf{r},-t|\mathbf{r}_1,-t_1)\frac{\partial}{\partial t}[\vec{\nabla}G_\beta(\mathbf{r},t|\mathbf{r}_0,t_0)]-G_\beta(\mathbf{r},t|\mathbf{r}_0,t_0)\frac{\partial}{\partial t}[\vec{\nabla}G_{-\beta}(\mathbf{r},-t|\mathbf{r}_1,-t_1)]\right)\cdot\vec{\mathbf{n}}ds. \tag{A5}$$

This vanishes by virtue of the homogeneous boundary conditions on G.

Turning next to the second integral in Eq. (A2), it is seen to be the integral of a total x derivative, and so vanishes because of the periodic boundary conditions. The third integral in Eq. (A2) can be rewritten, using Green's theorem (A4), as

$$\int_{-\infty}^{t_0^+} dt \oint [G_{-\beta}(\mathbf{r},-t|\mathbf{r}_1,-t_1)\vec{\nabla}G_\beta(\mathbf{r},t|\mathbf{r}_0,t_0)-G_\beta(\mathbf{r},t|\mathbf{r}_0,t_0)\vec{\nabla}G_{-\beta}(\mathbf{r},-t|\mathbf{r}_1,-t_1)]\cdot\vec{\mathbf{n}}ds,$$

which vanishes, again because of the homogeneous boundary conditions on G. Thus all terms on the left-hand side of Eq. (A2) vanish and Eq. (A1) is proved.

Using the reciprocity relation (A1), we can write an equation for $G(\mathbf{r},t|\mathbf{r}_0,t_0)$ as a function of $(\mathbf{r}_0,t_0)$:

$$-\frac{1}{C}\frac{\partial\nabla_0^2 G}{\partial t_0}-\frac{\beta}{C}\frac{\partial G}{\partial x_0}+\nabla_0^2 G=\delta^2(\mathbf{r}-\mathbf{r}_0)\,\delta(t-t_0) \tag{A6}$$

having suppressed the subscript β. Also, by Eq. (16),

$$\frac{1}{C}\frac{\partial\nabla_0^2\Psi_B(\mathbf{r}_0,t_0)}{\partial t_0}+\frac{\beta}{C}\frac{\partial\Psi_B(\mathbf{r}_0,t_0)}{\partial x_0}+\nabla_0^2\Psi_B(\mathbf{r}_0,t_0)=0. \tag{A7}$$

Multiplying Eq. (A6) by $\Psi_B(\mathbf{r}_0,t_0)$ and Eq. (A7) by G, subtracting, and integrating over the region of interest (northern hemisphere) and over t_0 from $-\infty$ to t^+, we obtain

$$-\frac{1}{C}\int_{-\infty}^{t^+}dt_0\int dx_0dy_0\left[\Psi_B(\mathbf{r}_0,t_0)\frac{\partial}{\partial t_0}\nabla_0^2G+G\frac{\partial}{\partial t_0}\nabla_0^2\Psi_B(\mathbf{r}_0,t_0)\right]-\frac{\beta}{C}\int_{-\infty}^{t^+}dt_0\int dx_0dy_0\left[\Psi_B(\mathbf{r}_0,t_0)\frac{\partial}{\partial x_0}G+G\frac{\partial}{\partial x_0}\Psi_B(\mathbf{r}_0,t_0)\right]$$
$$+\int_{-\infty}^{t^+}dt_0\int dx_0dy_0[\Psi_B(\mathbf{r}_0,t_0)\nabla_0^2G-G\nabla_0^2\Psi_B(\mathbf{r}_0,t_0)]=\Psi_B(\mathbf{r},t). \tag{A8}$$

The first term can be evaluated by integrating by parts in time, and using Green's theorem (A4) to write the resulting expression as a boundary integral, as in the derivation of Eqs. (A3) and (A5). In the present case this yields

$$\int_{-\infty}^{t^+}dt_0\int dx_0dy_0\left[\Psi_B(\mathbf{r}_0,t_0)\frac{\partial}{\partial t_0}\nabla_0^2G+G\frac{\partial}{\partial t_0}\nabla_0^2\Psi_B(\mathbf{r}_0,t_0)\right]$$
$$=\int dx_0dy_0[G\nabla_0^2\Psi_B(\mathbf{r}_0,t_0)]_{t_0=-\infty}^{t_0=t^+}+\int_{-\infty}^{t^+}dt_0\oint\left[\Psi_B(\mathbf{r}_0,t_0)\frac{\partial}{\partial t_0}\vec{\nabla}_0G-\frac{\partial}{\partial t_0}G\vec{\nabla}_0\Psi_B(\mathbf{r}_0,t_0)\right]\cdot\vec{\mathbf{n}}_0ds_0.$$

The upper limit in the first term on the right-hand side vanishes because of the causal boundary conditions on G, while the second term in the boundary integral vanishes because G satisfies homogeneous boundary conditions. [By reciprocity Eq. (A1), G vanishes for either $\mathbf{r}_0$ or $\mathbf{r}$ on the boundary.] Therefore

$$\int_{-\infty}^{t^+}dt_0\int dx_0dy_0\left[\Psi_B(\mathbf{r}_0,t_0)\frac{\partial}{\partial t_0}\nabla_0^2G+G\frac{\partial}{\partial t_0}\nabla_0^2\Psi_B(\mathbf{r}_0,t_0)\right]=-\int dx_0dy_0G(\mathbf{r},t|\mathbf{r}_0,-\infty)\nabla_0^2\Psi_B(\mathbf{r}_0,-\infty)$$
$$-\int_{-\infty}^{t^+}dt_0\oint\Psi_B(\mathbf{r}_0,t_0)\frac{\partial}{\partial t}(\vec{\nabla}_0G)\cdot\vec{\mathbf{n}}_0ds_0 \tag{A9}$$

having also used $\partial G/\partial t_0=-\partial G/\partial t$, which follows from the time-translation invariance of Eq. (24).

The second integral in Eq. (A8) is again the integral of a total x derivative, and so vanishes due to the periodic boundary conditions. The third integral is again reexpressed using Green's theorem (A4):

$$\int_{-\infty}^{t^+}dt_0\int dx_0dy_0[\Psi_B(\mathbf{r}_0,t_0)\nabla_0^2G-G\nabla_0^2\Psi_B(\mathbf{r}_0,t_0)]=\int_{-\infty}^{t^+}dt_0\oint[\Psi_B(\mathbf{r}_0,t_0)\vec{\nabla}_0G-G\vec{\nabla}_0\Psi_B(\mathbf{r}_0,t_0)]\cdot\vec{\mathbf{n}}_0ds_0. \tag{A10}$$

Since the second term in the integrand on the right-hand side of Eq. (A10) vanishes, with G, on the boundary, Eq. (A10) can be combined with the expression Eq. (A9) for the first integral in (A8), to yield finally

$$\int_{-\infty}^{t^+}dt_0\oint\Psi_B(\mathbf{r}_0,t_0)\left(1+\frac{1}{C}\frac{\partial}{\partial t}\right)(\vec{\nabla}_0G)\cdot\vec{\mathbf{n}}_0ds_0+\frac{1}{C}\int dx_0dy_0G(\mathbf{r},t|\mathbf{r}_0,-\infty)\nabla_0^2\Psi_B(\mathbf{r}_0,-\infty)=\Psi_B(\mathbf{r},t). \tag{A11}$$

The second term on the left-hand side represents the effects of conditions at initial time $t_0=-\infty$. This term vanishes, since $G\to0$ as $t-t_0\to\infty$, due to the dissipative term in Eq. (24). Equation (A11) is then of the form

$$\Psi_B(\mathbf{r},t)=\int_{-\infty}^{t}dt_0\oint ds_0\Psi_B(\mathbf{r}_0,t_0)G^b(\mathbf{r},t|\mathbf{r}_0,t_0),$$

where

$$G^b(\mathbf{r},t|\mathbf{r}_0,t_0)=\left(1+\frac{1}{C}\frac{\partial}{\partial t}\right)[\vec{\mathbf{n}}_0\cdot\vec{\nabla}_0G(\mathbf{r},t|\mathbf{r}_0,t_0)]. \tag{A12}$$

For the configuration depicted in Fig. 4, G^b is given by Eq. (26).

APPENDIX B: THE DEFINITION OF BLOCKING IN OBSERVED METEOROLOGICAL DATA

Blocking is commonly defined in terms of the *geopotential height* field $Z_P(x,y)$. Formally, at any pair of longitude and latitude coordinates (x,y):

$$Z_P(x,y)\equiv\frac{1}{g_0}\int_0^{p(x,y,z)=P}g(x,y,z)dz,$$

where $p(x,y,z)$ is the pressure at the same location at height z, g is the local gravitational constant, and g_0 is the mean surface gravitational constant. $Z_{500\,\mathrm{mbar}}$ is thus very nearly the physical height of the 500 mbar isobar. Z_{500} can also be thought of as a proxy for surface pressure in a roughly hydrostatic atmosphere.

We use the Tibaldi-Molteni diagnostic [36] to define blocking. To discount high-frequency transients, filtered heights are first defined as five-day averages, i.e.,

$\tilde{Z}_{500}(x,y,t) \equiv [1/(5\ \text{days})] \int_{t-2.5\ \text{days}}^{t+2.5\ \text{days}} Z_{500}(x,y,\tau)\, d\tau$, where the dependence of $Z_{500}(x,y,t)$ on time t has been indicated explicitly. We will say that the atmospheric circulation is blocked at a given location (x,y), if (x,y) is near a local maximum of $\tilde{Z}_{500}$ in latitude y, with a falloff rate on the poleward side that exceeds a prescribed threshold. Specifically, the atmosphere is said to be blocked at (x,y) in the northern hemisphere if and only if the two conditions

$$[\tilde{Z}_{500}(x,y+\delta) - \tilde{Z}_{500}(x,y+\delta-20^\circ)]/20^\circ > 0,$$

$$[\tilde{Z}_{500}(x,y+\delta) - \tilde{Z}_{500}(x,y+\delta+20^\circ)]/20^\circ > 10\ \text{m/deg}$$

are both met either for $\delta = 0^\circ$, $\delta = 5^\circ$, or $\delta = -5^\circ$. In the southern hemisphere, the right-hand sides of the two inequalities are interchanged.

[1] L. Pecora and T. Carroll, Phys. Rev. Lett. **64**, 821 (1990).
[2] H. Fujisaka and T. Yamada, Prog. Theor. Phys. **69**, 32 (1983).
[3] V. S. Afraimovich, N. N. Verichev, and M. I. Rabinovich, Radiophys. Quantum Electron. **29**, 795 (1986).
[4] N. F. Rulkov, M. M. Sushchik, and L. S. Tsimring, Phys. Rev. E **51**, 980 (1995).
[5] R. Brown, N. F. Rulkov, and N. B. Tufillaro, Phys. Lett. A **196**, 201 (1994); Phys. Rev. E **50**, 4488 (1994).
[6] T. L. Carroll and L. M. Pecora, Nav. Res. Rev. **3**, 4 (1993).
[7] J. M. Kowalski, G. L. Albert, B. K. Rhoades, and G. W. Gross, Neural Networks **5**, 805 (1992).
[8] T. L. Carroll, Biol. Cybern. **73**, 553 (1995).
[9] L. Kocarev, Z. Tasev, and U. Parlitz, Phys. Rev. Lett. **79**, 51 (1997).
[10] J. F. Heagy, T. L. Carroll, and L. M. Pecora, Phys. Rev. E **50**, 1874 (1994).
[11] R. Roy and K. S. Thornburg, Phys. Rev. Lett. **72**, 2009 (1994).
[12] H.E. de Swart, *CWI Tract 60: Vacillation and Predictability Properties of Low-order Atmospheric Spectral Models* (Stichting Mathematisch Centrum, Amsterdam, 1989); Acta Appl. Math. **11**, 49 (1988).
[13] P. J. Webster and J. R. Holton, J. Atmos. Sci. **39**, 722 (1982).
[14] J. Namias, J. Meteorol. **7**, 130 (1950).
[15] S. C. Venkataramani, B. R. Hunt, and E. Ott, Phys. Rev. E **54**, 1346 (1996).
[16] P. Ashwin, J. Buescu, and I. Stewart, Phys. Lett. A **193**, 126 (1994).
[17] N. Platt, E. A. Spiegel, and C. Tresser, Phys. Rev. Lett. **70**, 279 (1993).
[18] E. Ott and J. C. Sommerer, Phys. Lett. A **188**, 39 (1994).
[19] J. Brindley, T. Kapitaniak, and L. Kocarev, Geophys. Res. Lett. **22**, 1257 (1995).
[20] F. Rödelsperger, A. Čenys, and H. Benner, Phys. Rev. Lett. **75**, 2594 (1995).
[21] J. Pedlosky, *Geophysical Fluid Dynamics*, 2nd ed. (Springer-Verlag, Berlin, 1987).
[22] J. G. Charney and J. G. DeVore, J. Atmos. Sci. **36**, 1205 (1979).
[23] E. N. Lorenz, J. Atmos. Sci. **20**, 448 (1963).
[24] P. Hess and H. Brezowsky, *Katalog der Grosswetteranlagen Deutschlands* (Deutscher Wetterdienst, Bad Kissengen, 1969).
[25] B. Legras and M. Ghil, J. Atmos. Sci. **42**, 433 (1985).
[26] B. J. Hoskins and D. J. Karoly, J. Atmos. Sci. **38**, 1179 (1981).
[27] P.M. Morse and H. Feshbach, *Methods of Theoretical Physics* (McGraw-Hill, New York, 1953), pp. 795–803.
[28] P. J. Webster and H.-R. Chang, Dyn. Atmos. Oceans (to be published).
[29] E. M. Kalnay *et al.*, Bull. Am. Meteorol. Soc. **77**, 437 (1996).
[30] P. J. Webster and H. -R. Chang, J. Atmos. Sci. **45**, 804 (1988).
[31] G. T. Walker, Memoirs of the India Meteorological Department, **24**, Part 9, 275 (1924).
[32] J. Bjerknes, Tellus **18**, 820, (1966); Mon. Weather Rev. **97**, 163 (1969).
[33] J. M. Wallace and D. S. Gutzler, Mon. Weather Rev. **109**, 794 (1981).
[34] O. Morgul and M. Feki, Phys. Rev. E **55**, 5004 (1997).
[35] E. N. Lorenz, Nature (London) **353**, 241 (1991).
[36] S. Tibaldi and F. Molteni, Tellus **42A**, 343 (1990).